NCHRP 12-68

FY 2004

Rotational Limits for Elastomeric Bearings

Final Report

APPENDIX E

John F. Stanton

Charles W. Roeder

Peter Mackenzie-Helnwein

Department of Civil and Environmental Engineering

University of Washington

Seattle, WA 98195-2700

YOUR NOTES

TABLE OF CONTENTS

LIST OF FIGURES

LIST OF TABLES

APPENDIX E Finite Element Analysis

E.1 Introduction

The performed project focused mainly on the experimental investigation of the rotational behavior of elastomeric bearings and the development of suitable design procedures. This requires the identification of characteristic engineering design parameters which (1) can be measured in the experiment (direct or indirect), and (2) are reasonably simple to use for the routine design of bearings.

One key problem arising with experimental work is the selection of representative measures which can be tracked during testing. This restricts in-situ experimental observation to visible and measurable behavior on the surface of each tested bearing. Interior changes such as damage to the elastomer, permanent deformations in the steel shims and/or the elastomer, or damage to the interface between these components can only be observed post mortem, i.e. after the test program has finished. Local high strains in the interior of the bearing cannot be measured at all since a measurement would require modifications of the surface cover close to the end of the steel shims. This in turn would induce initial damage to exactly that portion of the bearing where initial debonding shall be used to identify the onset of structural damage to the bearing. These limitations of experimental procedures may result in observations which are often hard to interpret, and can void their relevance as a damage measure.

Finite element analysis (FEA) provides a tool to simulate structural behavior and assess internal states of deformation and stress. Using FEA enables us to correlate experimentally observed or controlled measures with local (internal) quantities. This benefit, however, is limited to the simulation of a well defined structure made of idealized homogeneous material. The level of accuracy depends on the type of material and the quality of available material properties. Despite this limitation, FEA is used to identify the relationship between external loads or applied displacements and rotations, and the engineering design parameters used in a design procedure. These relationships are then used to evaluate and justify simplified design equations.

The performed structural testing and evaluation of the experimental data identified the local shear strain γ_{zx} in the elastomer at (or near) the ends of the reinforcing steel shims as suitable engineering design parameter. Gent & Meinecke (1970) presented a simplified linear analysis for incompressible elastometric bearings. Stanton & Lund (2004) extended this theory for slightly compressible elastomers. Both formulations provide simple relations between axial force and average axial strain, as well as between moment and rotation. The shape of the bearings enters these relations solely through the shape factor *S* of the bearing. They also provide a convenient correlation between those global deformation measures and the local shear strain $\gamma_{zx,\max}$ inside the bearing. The linearity of the equations by Stanton & Lund (2004) provides an excellent basis for a design procedure. Their approach, however, utilizes superposition of axial and rotational loading and its validity has to be proven.

This chapter presents a numerical analysis by which the following hypotheses will be proven to hold for common bearings:

1. The *stiffness coefficients* predicted by the linear theory of bearings by Stanton & Lund are in good agreement with a nonlinear FEA.
2. The *local shear strain* predicted by the linear theory of bearings by Stanton & Lund are in good agreement with a nonlinear FEA.
3. *Superposition* of axial and rotational effects provides a reasonably accurate representation of the nonlinear FEA.
4. *Internal rupture* due to excessive tensile hydrostatic stress can only occur in bearings with bonded external plates and very low axial load intensities.

Proving these three hypotheses is of crucial importance for the justification for using the simple linear analysis by Stanton & Lund for design purposes.

E.2 Method and Model definition

E.2.1 Method

All nonlinear analysis presented in this chapter was performed using the multi-purpose Finite Element program MSC.Marc2003r2 by MSC.software. It provides a wide variety of specialized elements and material formulations. Through a long history of cooperation between MSC.software and the tire industry, MSC.marc2003r2 offers a good selection of material models for rubber and rubber-like materials.

Test simulations revealed that the commonly known problems of large deformation simulations of elastomers, i.e. extensive mesh distortion and the potential loss of element stability (visible as hourglass modes) impose a serious limitation on the numerical analysis.

Local mesh distortions are always observed near the end of the reinforcing steel shims. As loading progresses, mesh distortion inevitably results in inversion of elements and subsequent failure of the analysis. This limits the maximum axial compression and rotation which can be analyzed to average stresses of $\sigma = 2 - 3\,GS$ and rotations of 0.008-0.020 rad/layer.

Hourglass modes were observed in areas of a bearing where hydrostatic tension occurs. The performed analyses showed reliable results for hydrostatic tensile stresses (= positive values of mean normal stress) up to $\sigma = 3G = E$, with shear modulus G and Young's modulus E. This is approximately the magnitude described by Gent & Lindley (1958) for the generation of internal rupture. Hence, the FEA model can be used to assess critical hydrostatic tension in the bearings.

All analyses were performed on strip bearings using a large deformation plane strain analysis in a Lagrange setting. Three-dimensional analyses could not be performed at the necessary level of refinement due to numerical instabilities of the nearly incompressible element formulation at high hydrostatic stress.

E.2.2 Loading

One major consideration of creating the model was how to realistically portray the loading conditions. In all of the experimental tests the bearing was placed between two metal plates to ensure uniform loading. To simulate the experimental conditions the loading plates were represented using rigid surfaces and frictional contact between these surfaces and the bearings. The motion of the rigid loading surface can be controlled by defining the position (or velocity) of a reference point on the surface and an angle (or angular velocity) to identify its orientation. This requires the loading to be displacement controlled rather than, as desired, load controlled. The loading of the bearing was composed of slow axial compression to various levels of average axial strain ε_{az}, followed by rigid body rotation of the loading surface. Forces and moments on the loading surface, as well as local strain and stress measures were recorded for each load history.

In order to discuss the method used to define the model, there are three main aspects that will be considered. They are the geometry of the model and the boundary conditions, the material models, and the loading.

E.2.3 Geometry and boundary conditions

Bearings of various shape factor were considered in the numerical analysis. The most representative bearings were those with a cross section similar to the ones tested in the experimental program. An identical cross section as the tested 9 in x 22 in bearings with SF 6 yields a strip bearing with SF 9. (This is an effect of the different aspect ratio.) A model with SF 6 was generated by increasing the layer thickness from 0.5 in to 0.75 in. For validation purposes, a SF 12 bearing of the same type was obtained by reducing the layer thickness to 0.375 in.

All two-dimensional finite element models possess two symmetry planes. Due to the applied rotation, the loading patterns possess only one symmetry plane. The model utilizes the horizontal symmetry plane which both the bearing structure and the loading pattern have in common. This plane goes through the center of the bearing. Symmetry boundary conditions were applied on the symmetry plane.

Horizontal stability of the model was achieved through a very soft horizontal spring with vanishing stiffness once the loading surfaces are moved into contact with the bearing. This is necessary since the bearing will be held in place by friction on the loading surfaces but will move horizontally in the symmetry plane when rotation is applied at the loading surface. This would leave the bearing without horizontal support prior to contact with the loading surface except for the artificial soft spring.

Figure E-1, Figure E-2, and Figure E-3 show the geometry and the typically used Finite Element mesh for bearings with SF 6, SF 9, and SF 12, respectively. (Only top half modeled; not to scale.) The indicated reference point is used for shear strain analysis in sections E.4 and E.5.

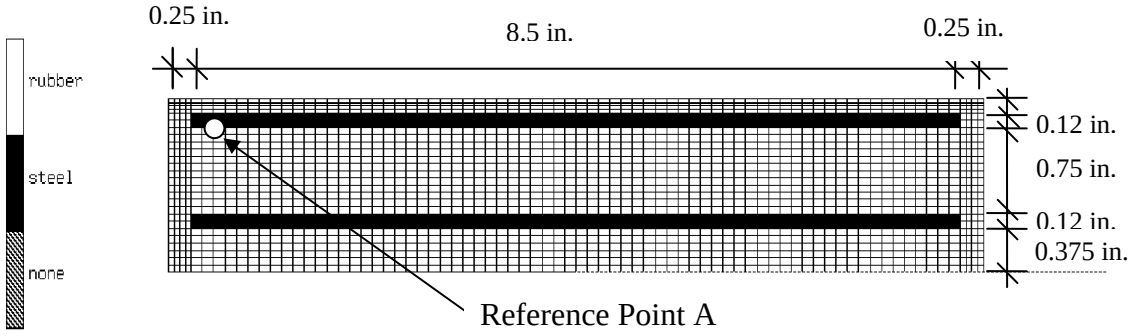

Figure E-1 Geometry and Finite Element mesh for a strip bearing with SF 6

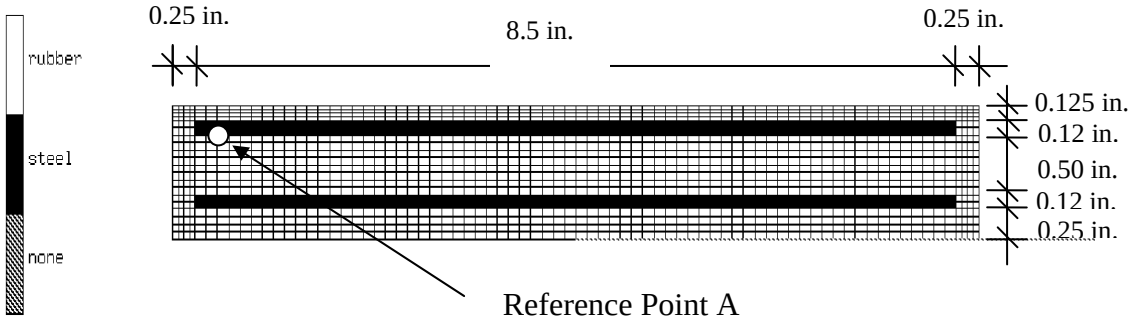

Figure E-2 Geometry and Finite Element mesh for a strip bearing with SF 9

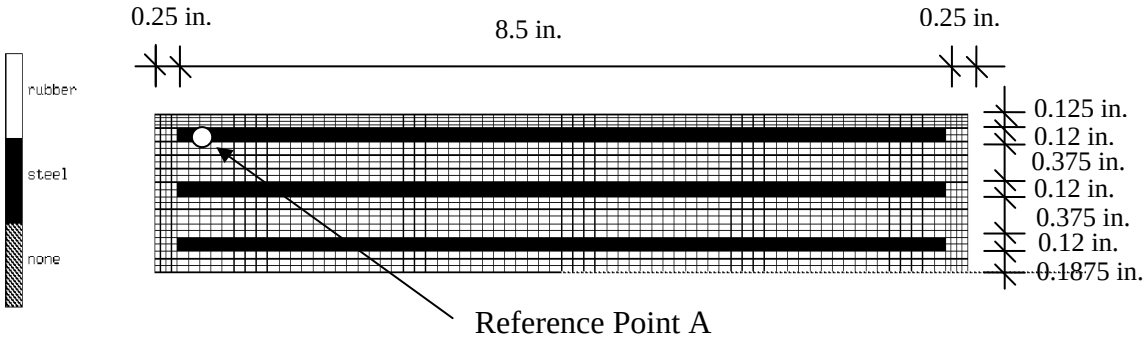

Figure E-3 Geometry and Finite Element mesh for a strip bearing with SF 12

Bearings with rigid or semi-rigid end-plates are modeled using the same mesh and loading but changing the interface properties from frictional contact to glue. This permanently attaches the bearing surface to the rigid loading surface and allows for identical load histories on bearings with and without rigid end-plates.

Elements representing elastomer were modeled using quadrilateral bi-linear elements with constant dilation, also known as Herrmann formulation [MSC.marc Manual A & B (2003)] (element type 80 in MSC.Marc2003r2). This formulation was designed for the analysis of incompressible and nearly incompressible material.

Elements representing the steels shims were modeled using quadrilaterals bi-linear shape functions with full integration (element type 11 in MSC.Marc2003r2). Tests on alternative integration schemes and mixed formulations produced no noticeable difference in the solution.

While the experimental data was collected and analyzed entirely using English system units, it was more convenient using metric units in the numerical analysis. The units used to run the analytical model in MSC.Marc2003r2 were meters (m) for length and Newton (N) for force, resulting in Pascal (Pa) for stress. These are the units on images and diagrams produced directly by MSC.marc2003r2. In order to analyze the data and to present comparisons with the linear theory by Stanton & Lund, the units were converted to the customary English system. That is, inches (in) were used for length, kilo-pounds (kips) for force, and kips per square inch (ksi) for stress.

E.2.4 Materials

The elastomer material was modeled as nonlinear elastic, nearly incompressible material. MSC.marc2003r2 provides the Ogden model, a generalized Mooney model, and the extension to the generalized Mooney model known as Gent's model [MSC.marc2003r2, manual A]. These models require between 8 and 12 parameters. Precisely speaking, the general Ogden model can be extended to any even number of parameters but MSC.marc2003r2 limits it for practical reasons [Ogden (1984)].

Bearing manufacturer on the other hand have to test their elastomer material and report Shore A hardness, elongation at failure and nominal stress at failure as the only parameters relevant for the 3D characterization of the elastic material. This presents a challenge and leaves space for variability on the manufacturer's side, and non-uniqueness of material parameters on the modeling part. Following a carefully justified suggestion by the project advisory group, the simplifying assumptions by Yeoh (1993) were adopted. Shore A hardness was used to estimate the shear modulus *G*. This parameter was later confirmed by shear tests performed on elastomer samples extracted from actual bearings. The bulk modulus *K* was obtained and later verified through a similar process. Parameters for Yeoh's model were obtained as follows.

First, a master tension test result was selected from the literature. This master curve is scaled linearly along the strain (or stretch) axis to match the ultimate elongation at break known from the manufacturer's testing. Then the stress axis is stretched by a linearly varying scaling function such that (a) the ultimate stress corresponds with the manufacturer's test, and (b) that the initial slope of the scaled curve (=uniaxial stiffness E_0) matches Young's modulus $E = 3G$ as identified from the Shore A hardness. This procedure makes sense since most materials used for elastomeric bearings have a very

similar *shape* of the uniaxial tension curve and differ mainly in few characteristic stiffness and strength values.

Second, Yeoh's model can be represented as a sensible subset of the generalized Mooney model and as such can be easily implemented in MSC.Marc2003r2. The work function for Yeoh's model is

$$W(\mathbf{E}) = C_{10}(I_1 - 3) + C_{20}(I_1 - 3)^2 + C_{30}(I_1 - 3)^3, \qquad \text{(E-1)}$$

where $\mathbf{E}$ is the Green-Lagrange strain tensor, $I_1 = \lambda_1{}^2 + \lambda_2{}^2 + \lambda_3{}^2 = \mathrm{tr}\,\mathbf{C}$ is the first invariant of the right Cauchy-Green strain tensor $\mathbf{C} = \mathbf{1} + 2\mathbf{E}$, and λ_i, $i = 1,2,3$ are the principal stretches. The 2nd Piola-Kirchhoff stress tensor follows from (E-1) as

$$\mathbf{S} = \frac{\partial W(\mathbf{E})}{\partial \mathbf{E}} + p\mathbf{C}^{-1} = \left[C_{10} + 2C_{20}(I_1 - 3) + 3C_{30}(I_1 - 3)^2\right]\frac{\partial I_1}{\partial \mathbf{E}} + p\mathbf{C}^{-1}, \qquad \text{(E-2)}$$

with the hydrostatic stress p to be determined from equilibrium equations.

Other stress measures follow from standard transformation rules. (See, e.g., Malvern (1969), Gurtin (1981), Ogden (1984), Marsden & Hughes (1983) for details.) Equation (E-2) can be specialized for uniaxial tension and leads to the engineering stress

$$\sigma = \frac{\text{Force}}{\text{Reference Area}} = 2\left[C_{10} + 2C_{20}(I_1{}^*) + 3C_{30}(I_1{}^*)^2\right]\left(\lambda_1 - \frac{1}{\lambda_1{}^2}\right). \qquad \text{(E-3)}$$

with

$$I_1{}^* = \lambda_1{}^2 + \frac{2}{\lambda_1} - 3. \qquad \text{(E-4)}$$

Equation (E-3) is used to identify the parameters C_{10}, C_{20}, C_{30}, using a least square fit of the scaled material test. The initial stiffness E_0 used to scale the reference material test is obtained as the initial slope of the stress-strain curve. It follows from (E-3) as

$$E_0 = \left.\frac{d\sigma}{d\lambda_1}\right|_{\lambda_1 = 1} = 6C_{10}. \qquad \text{(E-5)}$$

The following parameters were commonly used for the numerical analyses:

- shear modulus G = 100 psi (0.689 MPa),
- Bulk Modulus K = 400 ksi = 400,000 psi (2758 MPa),
- C_{10} = 344,470 Pa (49.961 psi),
- C_{20} = -6,216 Pa (0.901555 psi), and

- C_{30} = 292.09 Pa (0.042364 psi).

The steel shims in the bearings were A1011 Gr 36 steel. (Specification provided by an undisclosed manufacturer.) The material was modeled using isotropic, linear elastic-perfectly plastic J_2-plasticity (2D/3D *von Mises* material). The material properties used in the FEA were

- Young's Modulus E = 210 GPa (29,000 ksi),
- Poisson's ratio $\nu = 0.3$, and
- a yield stress of σ_Y = 235 MPa (34.1 ksi).

E.3 Evaluation and Validation of Stiffness Coefficients

Gent & Meinecke (1970) demonstrated that axial stiffness and rotational stiffness of bearings can be expressed in terms of shear modulus G and shape factor S. Introducing four coefficients A_{az}, B_{az}, A_{ry}, B_{ry} yields the following relations for the equivalent axial stiffness

$$E_{az} = 3G(A_{az} + B_{az}S^2) \tag{E-6}$$

and the effective bending stiffness

$$E_{ry}I = 3G(A_{ry} + B_{ry}S^2)I\,. \tag{E-7}$$

Stanton & Lund (2004) extended the formulation for slightly compressible material and proved that by properly adjusting the stiffness coefficients, the general form of equations (E-6) and (E-7) remains valid. They also showed that $A_{ax} = A_{ry} = \frac{4}{3}$ for all strip bearings.

The subscripts introduced by Gent & Meinecke (1970) and Stanton & Lund (2004) are used throughout Appendix E. However, for the sake of simplifying the notation, a simpler and more compact notation will be introduced and used in subsequent Appendices concerning design equations. For the reader's convenience, a list of equivalent symbols is given in Table E-1.

Table E-1 Stiffness coefficients used by Gent & Meinecke (1970) and Stanton & Lund (2004) and their simplified equivalent in the proposed design equations

Notation by Gent & Meinecke (1970) and Stanton & Lund (2004)	**Simplified (compacted) notation used in the proposed design equations**
A_{az}, B_{az}	A_a, B_a
A_{ry}, B_{ry}	A_r, B_r
C_{azzx}, C_{ryzx}	C_a, C_r

The aim of this section is to back-calculate these coefficients based on numerical results from nonlinear FEA. This will provide insight on both the significance of nonlinearity over the common load range for elastomeric bearings and on the potential model error of the linear theory by Stanton & Lund (2004).

E.3.1 Axial Stiffness Coefficient B_{az}

The bearing analysis is based on an infinite strip bearing. All simulations presented in this section were performed for axial compression only. Numerical instabilities limited the analyses to an average vertical stresses of $\sigma = 2 - 3\ GS$. Obtained numerical data represents the actual range of loading in real bearing applications, but lies below the experimentally applied load levels.

The numerical analysis provides force, displacements, local strains, and stresses. The displacement data is used to compute the average axial strain

$$\varepsilon_{az} = \frac{\delta_{top} - \delta_{bottom}}{t}, \tag{E-8}$$

where δ_{top} and δ_{bottom} are the vertical displacements of the shim on top and bottom, respectively, of the elastomer layer of thickness t. The average axial strain ε_{az} is positive if the bearing is compressed and negative if elongated. Force p as force per unit width of the bearing is then used to compute the equivalent stiffness coefficient

$$B_{az} = \frac{1}{S^2}\left(\frac{p}{EL\,\varepsilon_{az}} - A_{az}\right) \tag{E-9}$$

with L as the length of the bearing (= 9 in), $A_a = 4/3$, and

$$E = 3G\frac{1}{1 + G/3K} \approx 3G\,. \tag{E-10}$$

The error for using $E = 3G$ will be below 1 % for all common elastomers, and henceforth we will use the relation $E = 3G$ instead of (E-10).

E.3.1.1 Strip-bearing with SF 6

The bearing analysis is based on an infinite strip bearing as shown in Figure E-1 and dimensions as given in Table E-2. The analysis was performed for axial compression only. Numerical instabilities limited the analysis to an axial load of $P = 21.1$kips/in (or an equivalent of $P = 464$ kips on a 9 in x 22 in bearing).This represents an average stress of $\sigma = 1.98\,GS$.

Table E-2 Model parameters for SF 6 bearing

K	400,000 psi (2,760.0 MPa)
G	100 psi (0.690 MPa)
E	299.98 psi (2.068 MPa)
h.layer	0.750 in
n.layer	3
L	9 in

Figure E-4 shows the extracted secant value of B_{az} for SF 6 (S = 6.0) over the applied average axial strain, and compares it to the value obtained from Stanton & Lund (2004). The correlation is good and variations lie within 10-15 %. The reason for the difference can be explained by the simplifying assumption of an isotropic stress state in the theoretical analysis by Stanton & Lund versus a nonlinear plane strain analysis using the FEA. However, the value at zero axial strain, i.e., for the initial stiffness of the unloaded bearing, represents the only point where linear and nonlinear theories are expected to provide identical results. The difference can be explained from the difference between a real bearing with a ¼" cover layer and the idealized elastomer layer described by Stanton & Lund. Using the length of the shim (8.5 in) instead of the total length of the bearing (9.0 in) results in a theoretical shape factor of S = 5.67 instead of S = 6.0. This has some effect on the inverse calculation using (E-9) with results presented in Figure E-5.

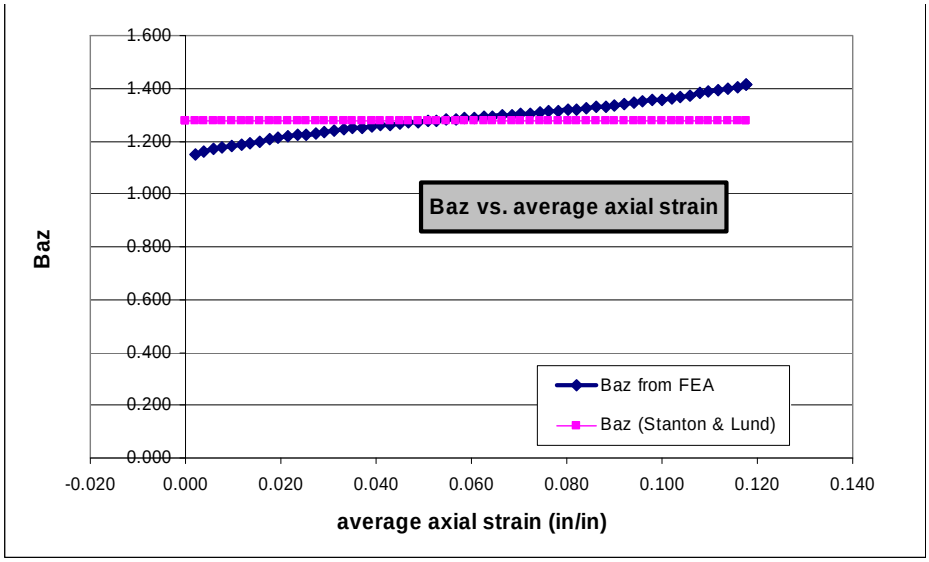

Figure E-4 B_{az} versus average axial strain for bearing with SF 6

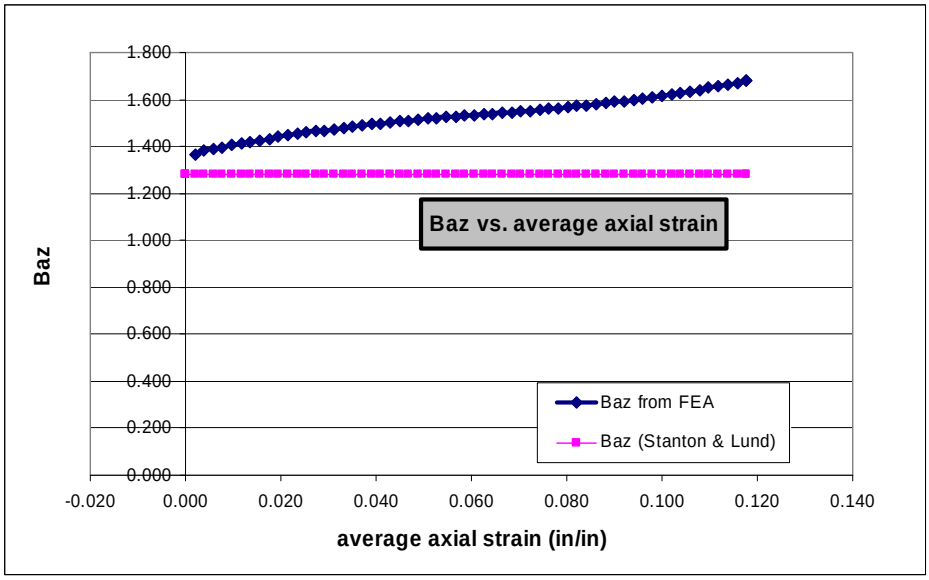

Figure E-5 B_{az} versus average axial strain for bearing with nominal SF 6 and calculation based on theoretical SF 5.67

Figure E-5 indicates that using the length of the shim for the computation of *S* yields better correlation for the stiffness of the unloaded bearing. However, subsequent nonlinear effects generate underestimation of the bearing stiffness up to 25 % as the axial load increases.

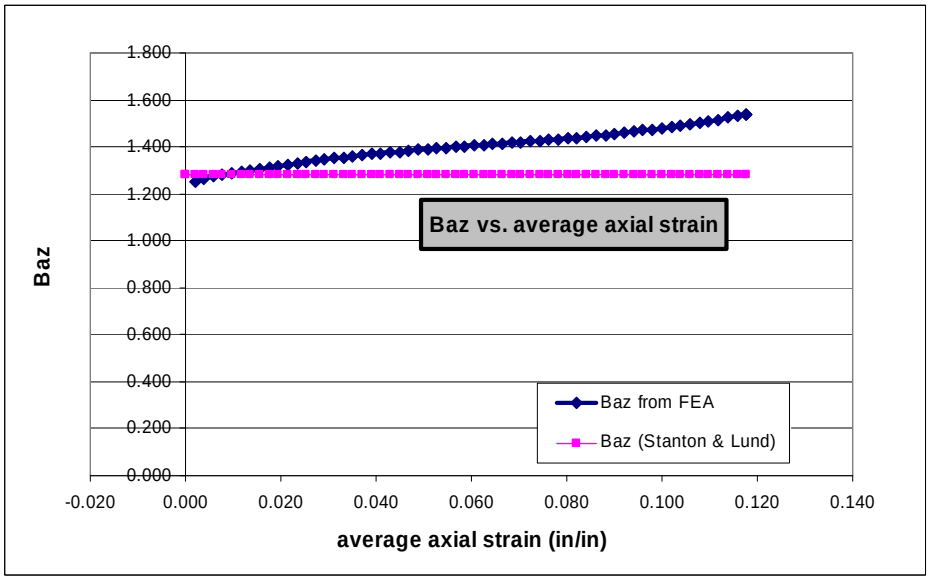

Figure E-6 B_{az} versus average axial strain for bearing with nominal SF 6 and calculation based on the average SF 5.83

Figure E-6 presents a back-calculation of B_{az} when using the average length of steel shim and total length of the bearing, leading to S = 5.83. This reduces the error for the loaded bearing without significant error at the unloaded state of the bearing.

The above analysis and comparison of Figure E-4 to Figure E-6 demonstrate that using the total length of the bearing when computing the shape factor results in a good balance of the model error over the common loading range of $\sigma = 0 - 2\ GS$. Using the actual length of the shim gives best results for the initial stiffness of the bearing but creates the largest model error as the axial strain, and thus the axial load increases.

E.3.1.2 Strip-bearing with SF 9

The bearing analysis is based on an infinite strip bearing as shown in Figure E-2 and dimensions as given in Table E-3. The analysis was performed for axial compression only. Numerical instabilities limited the analysis to an axial load of $P = 21.1\text{kips/in}$ (or an equivalent of $P = 464$ kips on a 9 in x 22 in bearing).This represents an average stress of $\sigma = 1.98\,GS$.

Table E-3 Model parameters for SF 9 bearing

K	400,000 psi (2,760.0 MPa)
G	100 psi (0.690 MPa)
E	299.98 psi (2.068 MPa)
h.layer	0.500 in
n.layer	3
L	9 in

Figure E-7 to Figure E-9 show the extracted secant value of B_{az} for SF 9 (S = 9.0) over the applied average axial strain, and compares it to the value obtained from Stanton & Lund (2004) for the same three ways of computing the shape factor as in the discussion of Figure E-4 to Figure E-6. The initial zero value for the back-calculated stiffness coefficient is an artifact of the way data was extracted from the FEA and has no physical relevance. The model error between linear and nonlinear analysis is still visible, though overall smaller than for SF 6 bearings. Moreover, its variation over the applied axial compression is significantly less that observed for SF 6.

The correlation between linear and nonlinear analysis is very good and variations lie within 0-10 %, except when using the length of the steel shim (Figure E-8) when the model error lies within 10-20 %. Using the full length of the bearing or the average length of shim and bearings for computing the shape factor result in equally good representation of the axial behavior (Figure E-7 and Figure E-9).

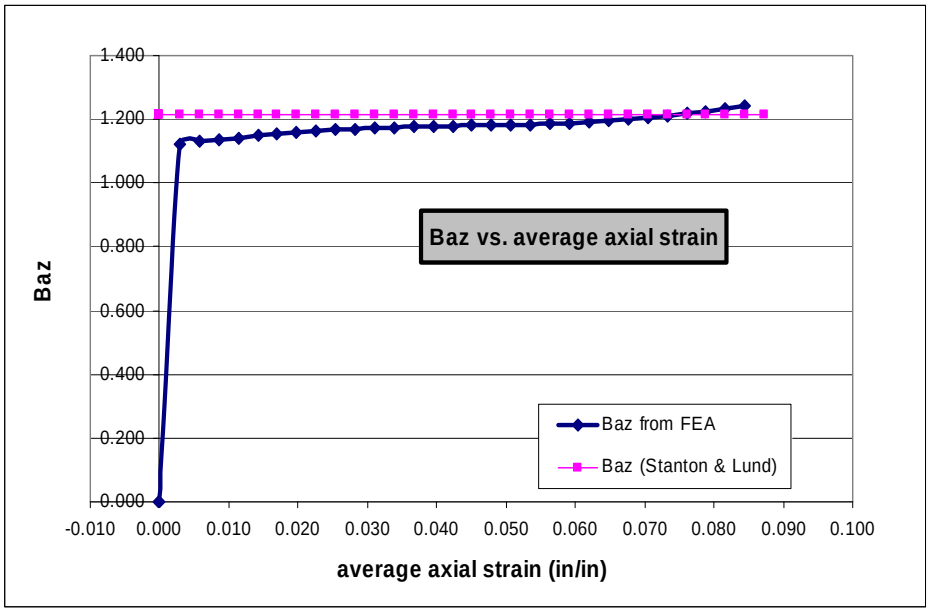

Figure E-7 B_{az} versus average axial strain for bearing with SF 9

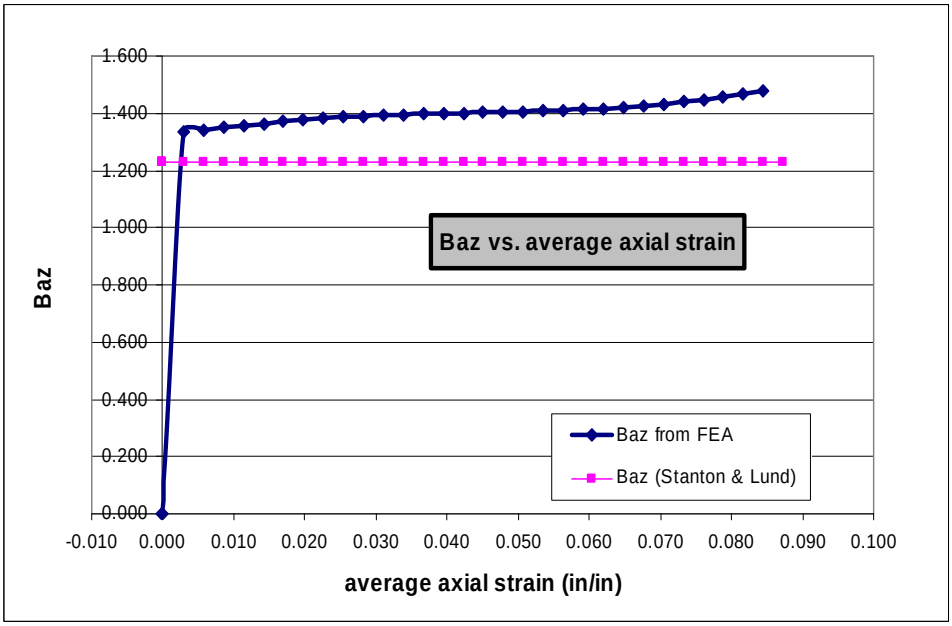

Figure E-8 B_{az} versus average axial strain for bearing with nominal SF 9 and calculation based on theoretical SF 8.50

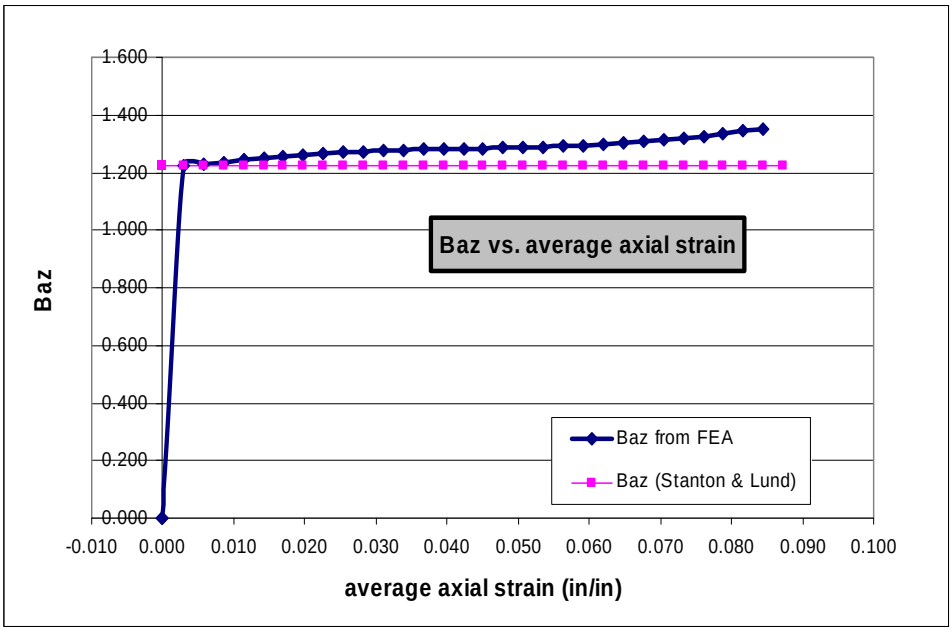

Figure E-9 B_{az} versus average axial strain for bearing with nominal SF 9 and calculation based on the average SF 8.75

E.3.1.3 Strip-bearing with SF 12

The bearing analysis is based on an infinite strip bearing as shown in Figure E-3 and dimensions as given in Table E-4. The analysis was performed for axial compression only. Numerical instabilities limited the analysis to an axial load of $P = 21.1$kips/in (or an equivalent of $P = 464$ kips on a 9 in x 22 in bearing). This represents an average stress of $\sigma = 1.98GS$.

Table E-4 Model parameters for SF 12 bearing

K	400,000 psi (2,760.0 MPa)
G	100 psi (0.690 MPa)
E	299.98 psi (2.068 MPa)
h.layer	0.375 in
n.layer	3
L	9 in

Figure E-10 shows the computed average stress (normalized by GS) versus the average axial compressive strain. The computed response shows almost perfectly linear response over the entire load history. Local mesh instabilities near the edge of the steel shims prevent a numerical analysis beyond the shown load level.

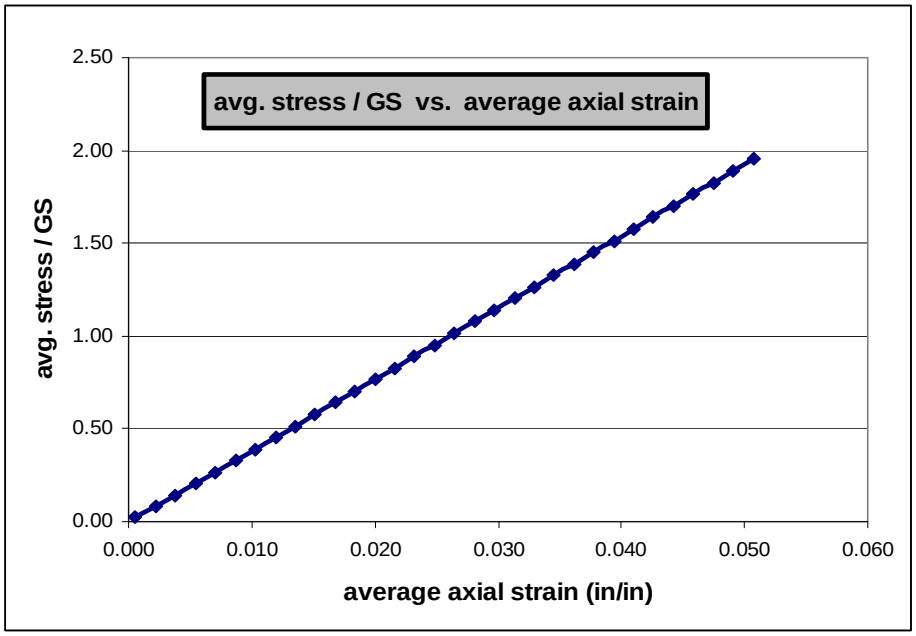

Figure E-10 σ / GS **versus average axial strain for bearing with SF 12**

Figure E-11 shows the obtained value for B_{az} as well as the theoretical value after Stanton & Lund (2004) over the applied load history. The equivalent stiffness coefficient obtained from the nonlinear FEA is almost constant, which translates to a virtually constant secant stiffness and a model error of 7.5 %. This observation further supports the hypothesis of linear behavior of SF 12 bearings at average stress levels of $\sigma \leq 2GS$.

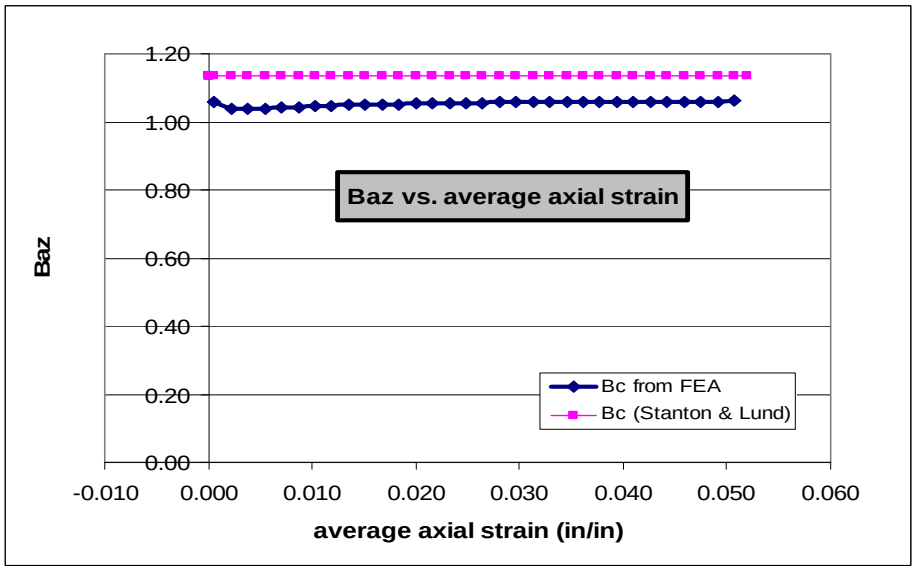

Figure E-11 B_{az} **versus average axial strain for bearing with SF 12**

Data presented in Figure E-11 is based on a shape factor calculated from the total length of 9.0 in which includes both shims and cover layer. Using solely the length of the shims

(i.e., 8.5 in) results in a theoretical shape factor of SF 11.33 for the same bearing. The graph in Figure E-12 shows results of a similar analysis as used for data in Figure E-11 but based on the theoretical shape factor of SF 11.33. Both figures clearly demonstrate that using the width of the shim and the total width of the bearing, respectively, for the definition of the shape factor, the linear theory by Stanton & Lund yields lower and upper bounds for the bearing stiffness.

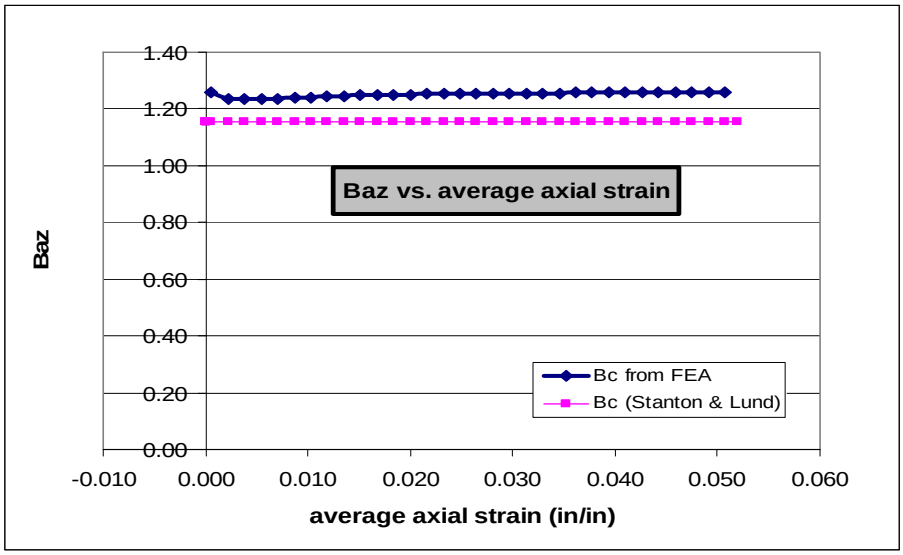

Figure E-12 B_{az} **versus average axial strain for bearing with nominal SF 12 and calculation based on theoretical SF 11.33.**

Using the average length of shim and that of the real bearing for computing the shape factor, results in SF 11.67 and a stiffness coefficient as shown in Figure E-13. Basing the shape factor on the average length of the bearing clearly achieves the best correlation between linear theory and nonlinear FEA at low to moderate axial load.

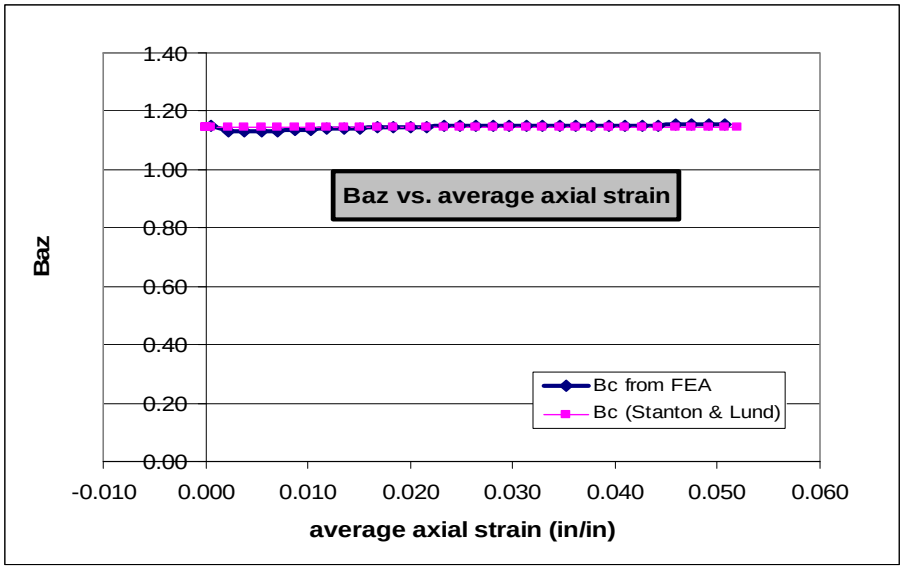

Figure E-13 B_{az} versus average axial strain for bearing with nominal SF 12 and calculation based on the average SF 11.67.

E.3.1.4 Summary for the axial stiffness coefficient B_{az}

The stiffness coefficient B_{az} was analyzed for three types of bearings with SF 6, SF 9, and SF 12. The listed shape factors are nominal shape factors computed using the total length of the bearing (= 9.0 in). The analytical equations by Stanton & Lund, however, are based on bearings without cover layer. To assess the significance of the cover layer for the computation of the axial stiffness of a bearing, the identification of B_{az} from the numerical analysis was based on three different ways of computing the shape factor:

1. Using the total lengths of the bearing, i.e. including the cover layer (L = 9.0 in),
2. Using the actual length of the shim (L = 8.5 in), and
3. Using the average of shim length and total length of the bearing (L = 8.75 in).

This leads to three different coefficients for each bearing if based on the linear theory. For the actual nonlinear analysis, B_{az} becomes a function of average axial strain ε_{az} or of relative applied load $P / AGS = p / LGS = \sigma / GS$.

Table E-5 presents a summary of the obtained stiffness coefficients.

Table E-5 Comparison of stiffness coefficient B_{az} for modified definitions of *S*

Nominal S	l (in)	h (in)	S	lambda	Baz (Stanton & Lund)	Baz (FEA at 0*GS)	Error (%)	Baz (FEA at 1GS)	Error (%)
6	9.000	0.750	6.00	0.1643	1.28	1.15	11.2	1.26	1.2
6	8.750	0.750	5.83	0.1598	1.28	1.25	2.3	1.37	-6.6
6	8.500	0.750	5.67	0.1552	1.28	1.37	-6.1	1.49	-14.1
9	9.000	0.500	9.00	0.2465	1.22	1.12	8.2	1.17	3.6
9	8.750	0.500	8.75	0.2396	1.22	1.22	-0.1	1.27	-4.1
9	8.500	0.500	8.50	0.2328	1.23	1.33	-8.0	1.39	-11.7
12	9.000	0.375	12.00	0.3286	1.14	1.05	7.9	1.06	7.7
12	8.750	0.375	11.67	0.3195	1.15	1.15	-0.1	1.15	-0.1
12	8.500	0.375	11.33	0.3104	1.16	1.25	-7.6	1.26	-7.9

The error value gives the relative error of the linear analysis under the assumption that the nonlinear analysis defines the correct answer. Due to the variability of the secant stiffness from the nonlinear solution, this error varies. Thus, in Table E-5 the relative error is presented first at zero load, and second at $\sigma = 1.0\ GS$. Best results for each combination are indicated by shaded fields. In most cases, the best correlation between the linear theory by Gent & Meinecke (1970), and Stanton & Lund (2004) and the present nonlinear analysis is obtained when using the average length of the bearing and the shim for computing the shape factor. Using the linear theory and basing the shape factor on the total length of the bearing results in overestimation of axial stiffness by the linear theory, while using the true length of the shims underestimates the axial stiffness of the bearing.

Nonlinear effects become more significant as the shape factor decreases. No significant nonlinear effect is observed over the given range of loads for SF 12. This statement, however, is only supported for load levels of $\sigma < 2.0\ GS$ on SF 12 bearings, and $\sigma < 3.0\ GS$ on SF 6 bearings. Excessive mesh distortion prevents further simulation, but also indicates significant changes in the load bearing mechanism. Experimental evidence clearly demonstrates that the finding of this section do not hold for much higher load levels.

E.3.2 Bending Stiffness Coefficient B_{ry}

Stanton & Lund (2004) showed that the moment-rotation relation for elastomeric bearings can be expressed as

$$M_y = 3G\,I(A_{ry} + B_{ry}S^2)\frac{\theta_y}{\sum t} = EI(A_{ry} + B_{ry}S^2)\frac{\theta_y}{\sum t}, \qquad \text{(E-11)}$$

where M_y is the total moment on the bearing, EI its linear elastic bending stiffness, A_{ry} and B_{ry} are stiffness coefficients, S is the shape factor, θ_y the total rotation on the bearing, and $\sum t$ is the total thickness of all rubber layers (provided they do have identical layer thickness). Solving (E-11) for B_{ry} yields

$$B_{ry} = \left(\frac{M_y}{EI}\frac{\sum t}{\theta_y} - A_{ry}\right)\frac{1}{S^2}. \qquad \text{(E-12)}$$

For infinite strip bearings, Stanton & Lund (2004) showed that $A_{ry} = 4/3$, effectively reducing (E-12) to

$$B_{ry} = \left(\frac{12\,M_y}{E\,W L^3}\frac{\sum t}{\theta_y} - \frac{4}{3}\right)\frac{1}{S^2} = \left(\frac{12\,m_y}{E\,L^3}\frac{\sum t}{\theta_y} - \frac{4}{3}\right)\frac{1}{S^2}, \qquad \text{(E-13)}$$

with $m_y = M_y / W$ as moment per unit width, *W*, of the bearing.

Equation (E-13) is used for the identification of B_{ry} from nonlinear FE analyses of bearings. It could be applied in its total form yielding an equivalent linear secant stiffness, or in an incremental manner yielding a tangent stiffness coefficient. The secant formulation was chosen in order to obtain linear relations for the design procedure.

The following four subsections summarize the findings from a series of analyses of a SF 9 bearings with rigid end-plates. The aim of this sequence is to answer the question whether or not the rotational stiffness depends on the applied axial load, or if the variability (if any were observed) is sufficiently small to justify the use of a linear analysis in a design procedure. This is achieved by studying four distinct load histories for the same bearing.

E.3.2.1 Strip-bearing with SF 9 – Rotation at $\sigma = 0.0\,GS$

During the first sequence, rotation was applied to the bearing without any initial axial load applied to the bearing. The simulated moments were recorded, and B_{ry} was computed using equation (E-13). Following identical arguments as presented in section E.3.1, evaluation was performed for SF 9 (= outer length/2 *t*), SF 8.5 (= length of shim/2 *t*), and SF 8.75 (= average length/2 *t*). Figure E-15, Figure E-16, and Figure E-17 show the results from the respective back-calculation versus the value predicted by the linear theory of Stanton & Lund.

The nonlinear analysis shows a constant stiffness coefficient for $\theta_y / n < 0.0065$ rad/layer which indicates perfectly linear behavior. The stiffness appears to change rapidly for $\theta_y / n > 0.0065$ rad/layer. A simple visual inspection of the computed deformation pattern in that regime reveals a significant hourglass mode pattern over that half of the bearing which is subjected to tension (marked area). Hence, the numerically obtained values are only valid for $\theta_y / n < 0.0065$ rad/layer. Figure E-14 shows the deformed FE model at a rotation of $\theta_y = 0.070$ rad on the full bearing. The right (tensile) side of the bearing shows the typical hourglass mode pattern.

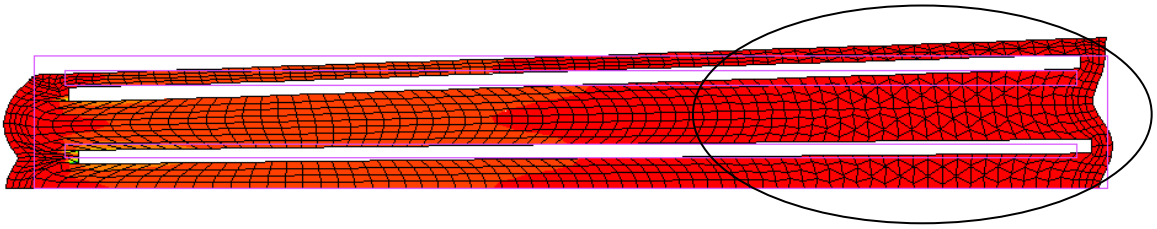

Figure E-14 Hourglass modes distorting the right side of a bearing with bonded external plates subjected to rotation only

The analysis shows that a shape factor based on the average length of shim and bearing yields the best correlation at virtually zero model error. Both of the other strategies result in a model error of up to +/-18 %.

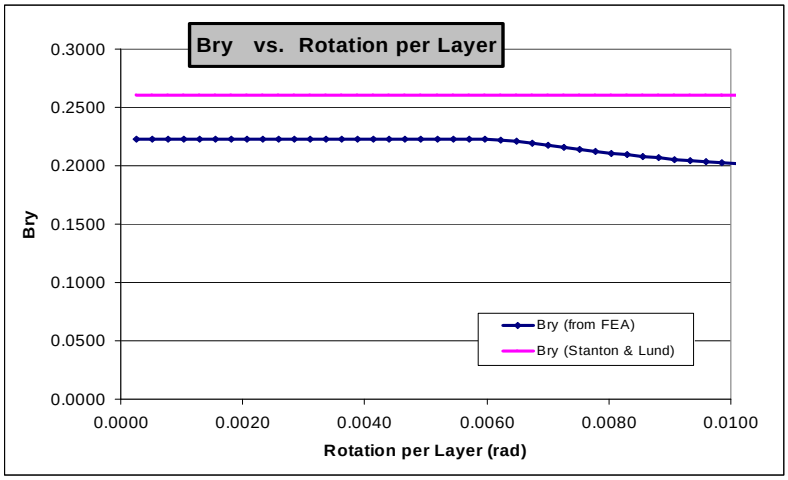

Figure E-15 B_{ry} **versus average axial strain for bearing with SF 9 at** ***P*** **= 0**

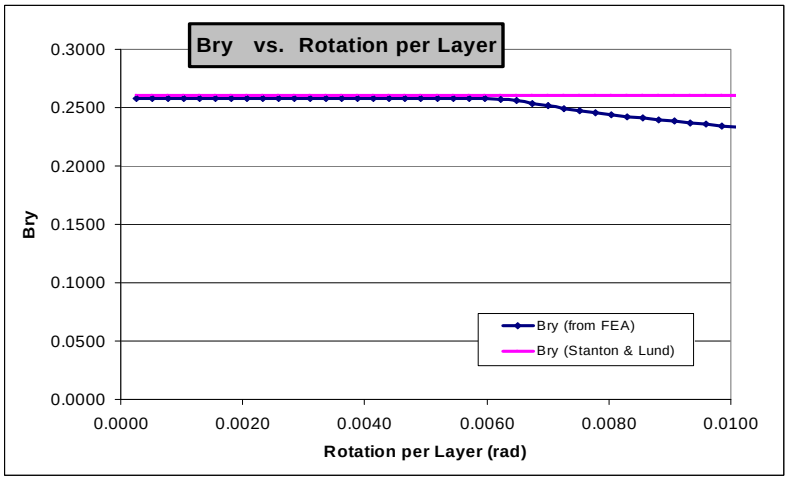

Figure E-16 B_{ry} **versus average axial strain for bearing with nominal SF 9 and calculation based on theoretical SF 8.75 at** ***P*** **= 0**

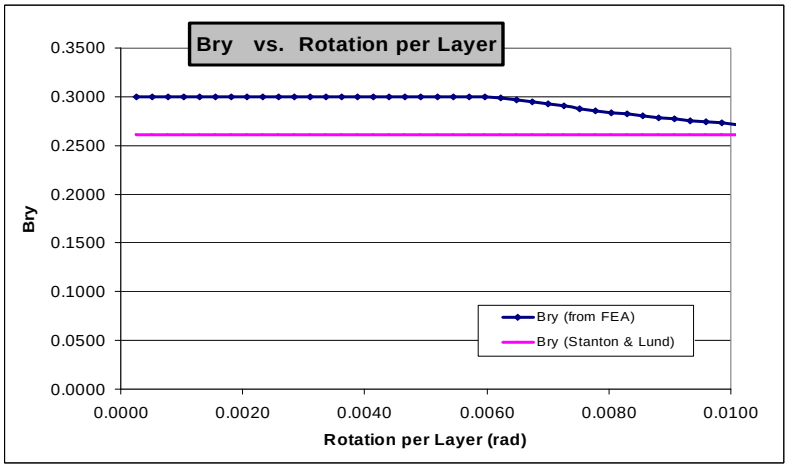

Figure E-17 B_{ry} **versus average axial strain for bearing with nominal SF 9 and calculation based on theoretical SF 8.50 at** ***P*** **= 0**

E.3.2.2 Strip-bearing with SF 9 – Rotation at $\sigma = 1.0\,GS$

During the second sequence, an axial load of $P = \sigma A = 1.0\ GS\ A$ was applied before rotating the bearing. The simulated moments were recorded and B_{ry} was computed using equation (E-13). Figure E-18, Figure E-19, and Figure E-20 show the results based on SF 9, SF 8.75, and SF 8.5, respectively.

The nonlinear analysis shows a constant stiffness coefficient for $\theta_y / n < 0.0065$ rad/layer which indicates perfectly linear behavior. The stiffness appears to change rapidly at $\theta_y / n > 0.0065$ rad/layer. An analysis of the computed deformation pattern in that regime again reveals significant hourglass mode patterns over that half of the bearing which is subjected to tension. Hence, the numerically obtained values are only valid for $\theta_y / n < 0.0065$ rad/layer.

The analysis shows that a shape factor based on the total length or on the average length of shim and bearing yields the best correlation at less than 10 % model error. Computing the shape factor based on the length of the shim results in a model error of 20 %.

E.3.2.3 Strip-bearing with SF 9 – Rotation at $\sigma = 1.5\,GS$

During the third sequence, an axial load of $P = \sigma A = 1.5\ GS\ A$ was applied before rotating the bearing. The simulated moments were recorded and B_{ry} was computed using equation (E-13). Figure E-21, Figure E-22, and Figure E-23 show the results based on SF 9, SF 8.75, and SF 8.5, respectively.

The nonlinear analysis shows a very slightly increasing stiffness coefficient for the entire range of θ_y / n. No hourglass mode patterns develop under these loading conditions.

The analysis shows that a shape factor based on the total length or on the average length of shim clearly yields the best correlation at 0-7 % model error. Basing the shape factor on the length of the shim results in a model error of 40 % and thus linear analysis significantly underestimates the rotation stiffness if the wrong shape factor is used in the analysis.

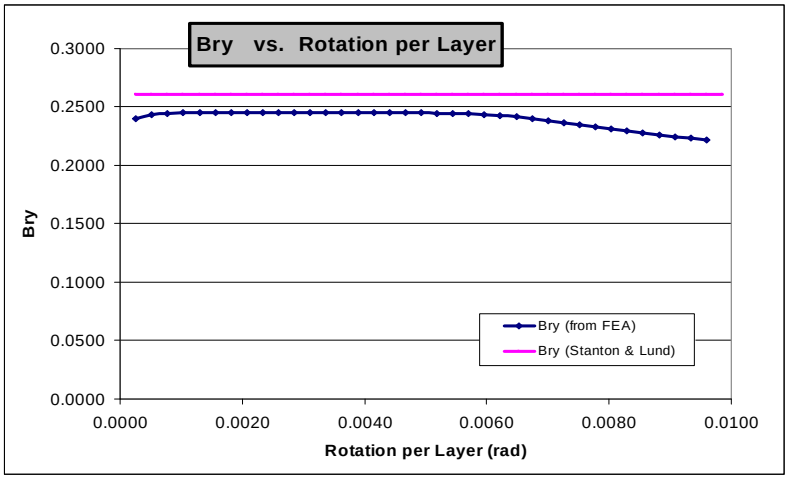

Figure E-18 B_{ry} **versus average axial strain for bearing with SF 9 at *P = 1.0 GS A***

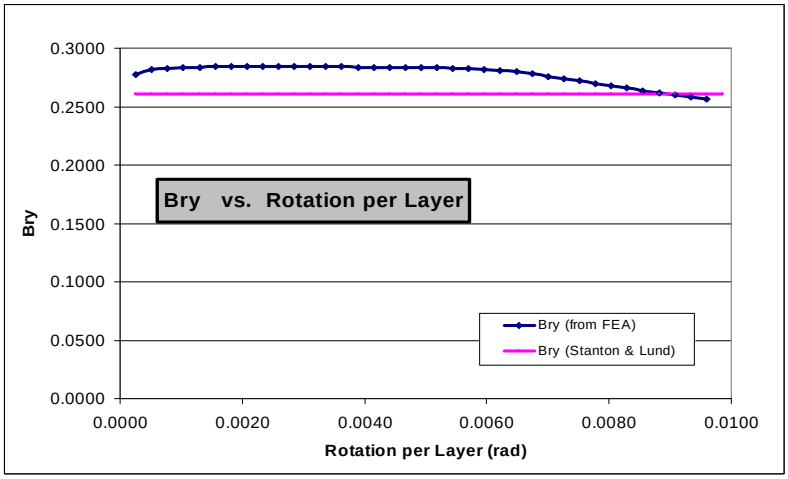

Figure E-19 B_{ry} **versus average axial strain for bearing with nominal SF 9 and calculation based on theoretical SF 8.75 at *P = 1.0 GS A***

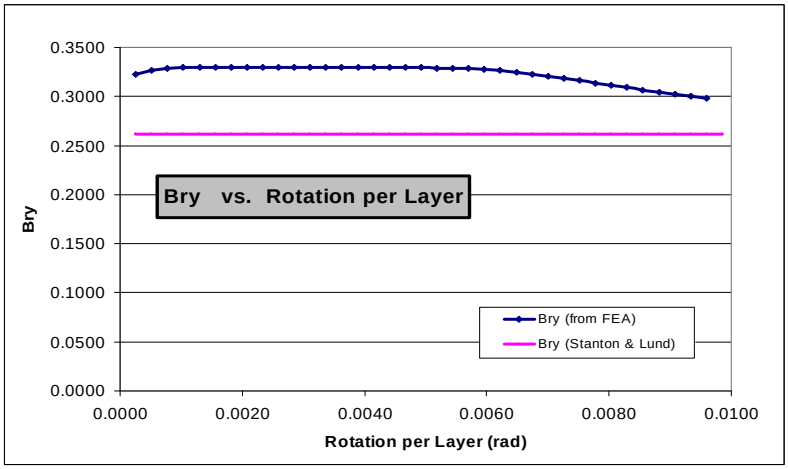

Figure E-20 B_{ry} **versus average axial strain for bearing with nominal SF 9 and calculation based on theoretical SF 8.50 at *P = 1.0 GS A***

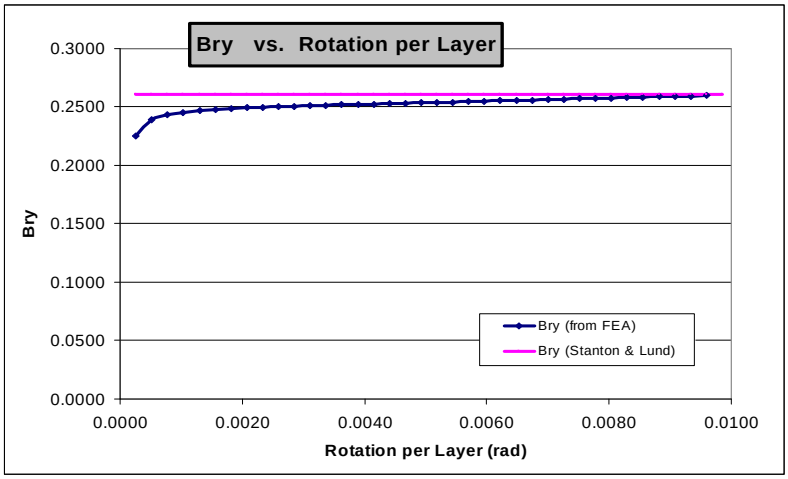

Figure E-21 B_{ry} **versus average axial strain for bearing with SF 9 at *P = 1.5 GS A***

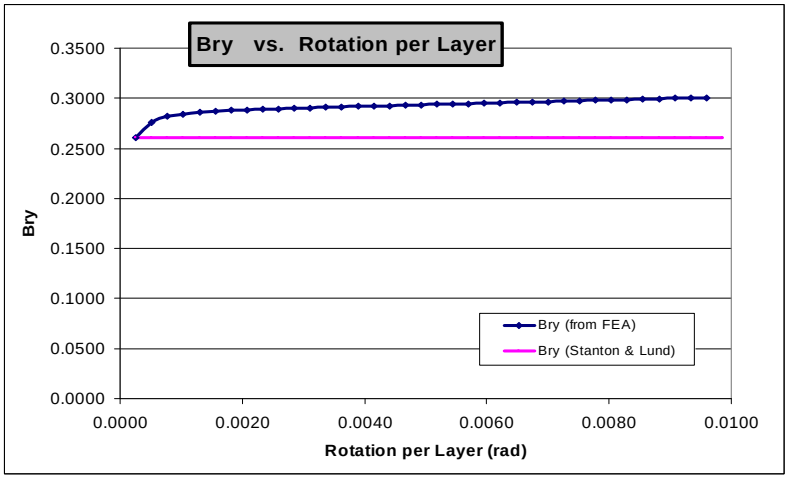

Figure E-22 B_{ry} **versus average axial strain for bearing with nominal SF 9 and calculation based on theoretical SF 8.75 at *P = 1.5 GS A***

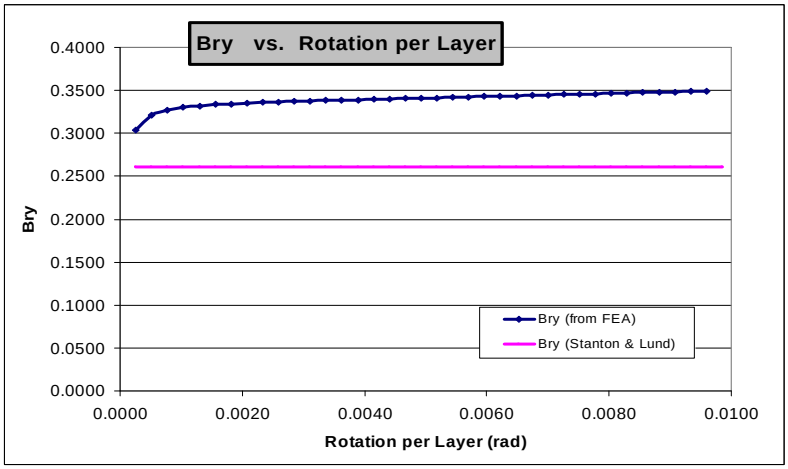

Figure E-23 B_{ry} **versus average axial strain for bearing with nominal SF 9 and calculation based on theoretical SF 8.50 at *P = 1.5 GS A***

E.3.2.4 Strip-bearing with SF 9 – Rotation at $\sigma = 1.85\,GS$

During the forth sequence, an axial load of $P = \sigma A = 1.85\ GS\ A$ was applied before rotating the bearing. This represents the highest load for which a numerically stable solution can be obtained for the presented level of rotation. The simulated moments were recorded and B_{ry} was computed using equation (E-13). Figure E-24, Figure E-25, and Figure E-26 show the results based on SF 9, SF 8.75, and SF 8.5, respectively.

The nonlinear analysis shows a very slightly increasing stiffness coefficient for the entire range of θ_y / n. No hourglass mode patterns develop under these loading conditions.

The analysis shows that a shape factor based on the total length or on the average length of shim clearly yields the best correlation at 0-10 % model error. Basing the shape factor on the length of the shim results in a model error of 40 % and thus linear analysis significantly underestimates the rotation stiffness if the wrong shape factor is used in the analysis.

Neither the numerical results for B_{ry}, nor the error analysis shows any significant difference between a load level of $P = \sigma A = 1.5\ GS\ A$ and $P = \sigma A = 1.85\ GS\ A$.

E.3.2.5 Summary for the rotational stiffness coefficient B_{ry}

The stiffness coefficient B_{ry} was analyzed for four different combinations of axial compression and simultaneous rotation. Back-calculation was performed for three different definitions of the shape factor: (a) using the full length of the bearing, (b) using the average between the length of the shim and the full length of the bearing, and (c) using the length of the steel shim to compute $S = A_{loaded} / A_{surface} = L / 2t$ .The analysis shows that (1) using the full length of the bearing, i.e. including the surface cover for the definition of S yields best results for axially loaded bearings, (2) the model error decreases as the axial load increases, and (3) using the length of the steel shim for the computation of S can cause significant underestimation of the rotational stiffness.

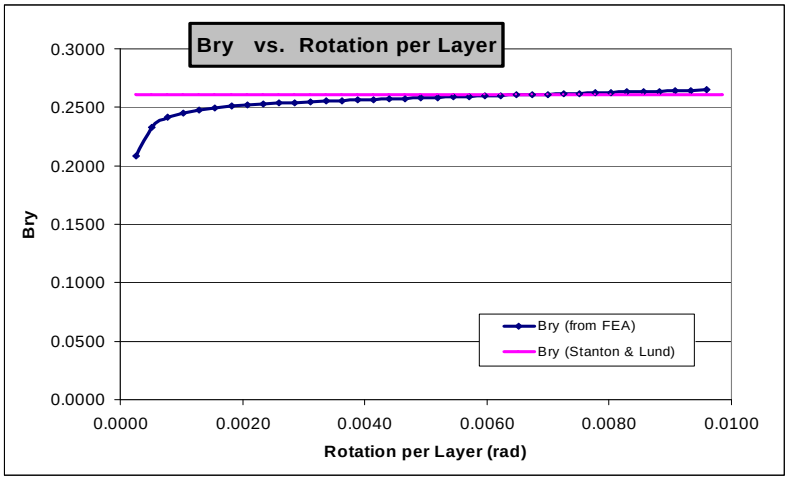

Figure E-24 B_{ry} **versus average axial strain for bearing with SF 9 at *P = 1.89 GS A***

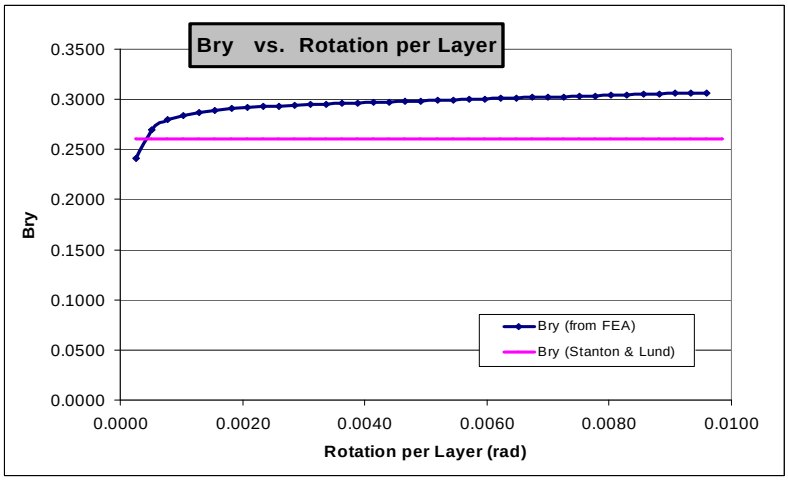

Figure E-25 B_{ry} **versus average axial strain for bearing with nominal SF 9 and calculation based on theoretical SF 8.75 at *P = 1.89 GS A***

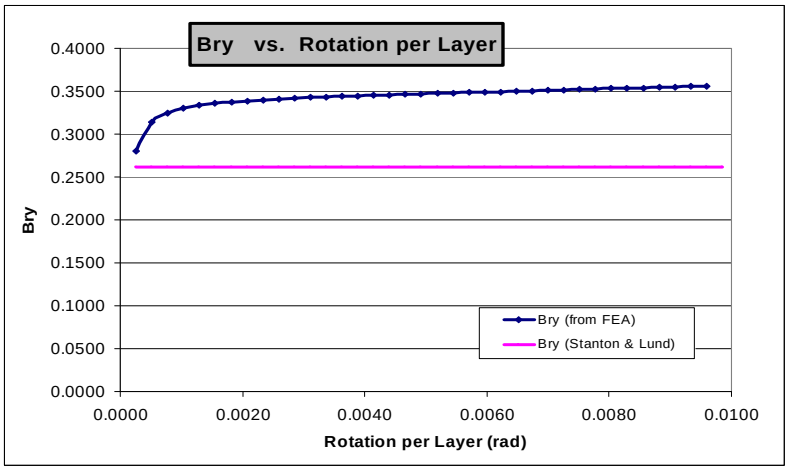

Figure E-26 B_{ry} **versus average axial strain for bearing with nominal SF 9 and calculation based on theoretical SF 8.50 at *P = 1.89 GS A***

E.4 Evaluation of Local Shear Strain for Design Purposes

Development of a reliable design procedure while maintaining reasonably low complexity of the required analysis requires

1. a simple mechanical quantity to correlate experimental data,
2. a compact and universal relation to compute that measure, and
3. validation of the procedure against higher order (nonlinear) models.

The theories by Gent & Meinecke (1970), and Stanton & Lund (2004) provide a suitable formulation to satisfy requirement 2, and at the same time suggest $\gamma_{zx,\max}$ in the elastomer at the end of the shims as the answer to requirement 1. This section will satisfy requirement 3, leaving the answer for the special case of lift-off to section E.5.

E.4.1 Local Effects at the End of the Steel Shims

Various levels of mesh refinement were applied to study local effects near the end of the steel shims. The shims were modeled deformable as mild steel with material parameters as given in subsection E.2.4. Very large strains are observed in the elastomer locally near the edge of the shim. The shim itself behaves almost rigid and remains elastic throughout the analysis. Using a linear theory, the sharp edge of the shim will introduce a singularity. Thus, the numerical analysis cannot provide sufficiently high resolution of that local area to provide actual numbers at the very edge of the shim. The shape of real edges of shims varies between manufacturers from sharp cuts to sanded (slightly rounded). Both the numerical limitations and the variability of the real product require some special consideration when analyzing and comparing numerical data and results from a linear analysis. This subsection contains a brief discussion of special phenomena observed at the ends of the steel shims. Based on these relations, a strategy for the subsequent analysis is developed.

Figure E-27 and Figure E-28 show the distribution of shear strain $\gamma_{zx} = 2E_{12}$, with E_{12} as the in-plane shear component of Green-Lagrange strain. Only deformation and strain in the elastomer are shown. The undeformed mesh primarily consists of perfectly horizontal and vertical parallel element boundaries. The deformed mesh shows the magnitude of local shear strain even at relatively small axial loads of $\sigma = 0.52\,GS$ (Figure E-27) and $\sigma = 1.02\,GS$ (Figure E-28). The figures clearly illustrate that elastomer is squeezed out of the parallel layers and subsequently is pushed around the edge of the steel shim in a mode of lateral expansion of the elastomer layer. Eventually, this very local mode of deformation causes the large strains leading to massive mesh distortion and failure of the numerical analysis. However, the parabolic distribution of horizontal displacements as postulated by the theoretical approach by Gent & Meinecke and also used by Stanton & Lund remains valid at a distance of ≥ 0.1 in from the edge of the shim.

At $\sigma = 0.52\,GS$, shear strain reaches extreme values over the last 0.05 in of the shim (Figure E-27). At $\sigma = 1.02\,GS$, extreme values of shear strain are found concentrated at the edge and to both sides of it (Figure E-28).

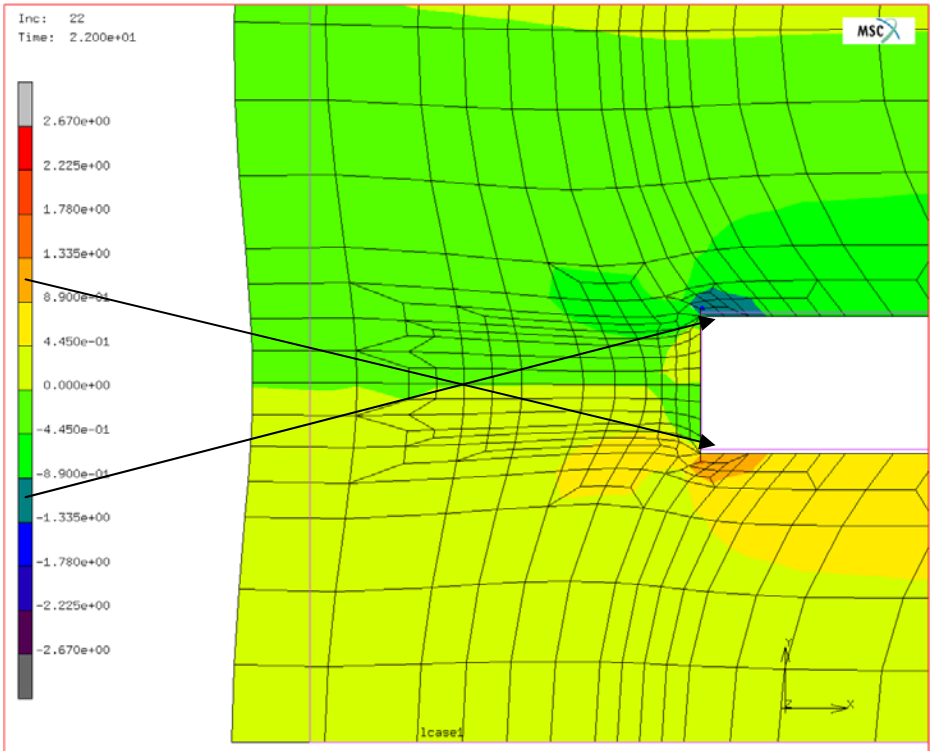

Figure E-27 Computed shear strain $\gamma = 2E_{12}$ in (in/in) at $\sigma = 0.52\,GS$ at the edge of a steel shim.

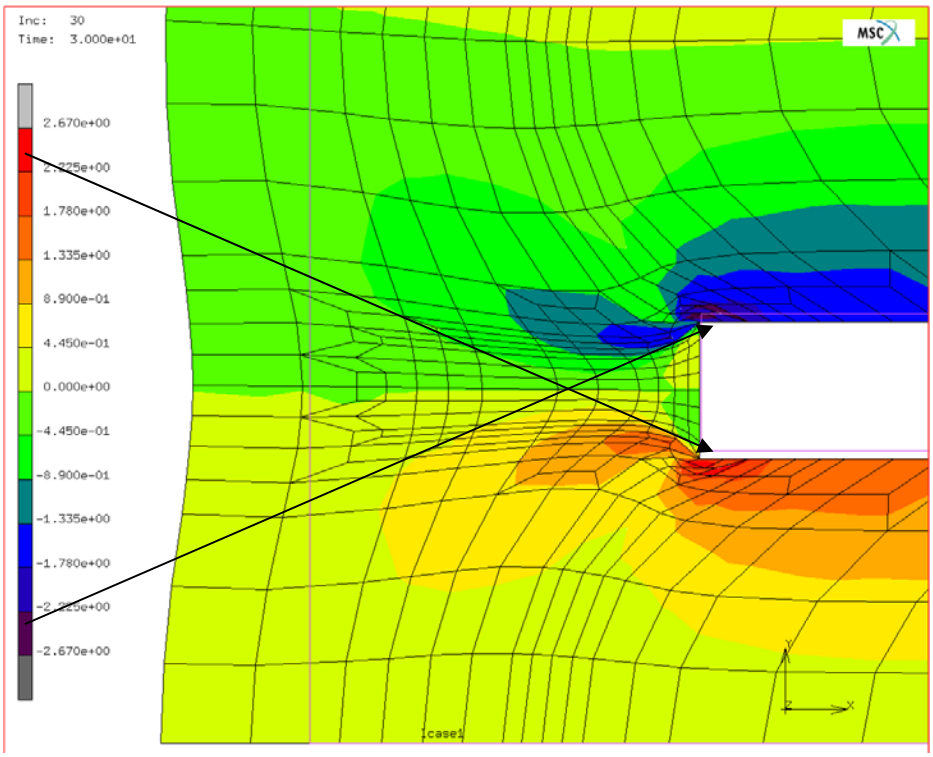

Figure E-28 Computed shear strain $\gamma = 2E_{12}$ in (in/in) at $\sigma = 1.02\,GS$ at the edge of a steel shim.

As the deformation increases, the effect of lateral expansion of the elastomer becomes the dominant mechanism in the vicinity of the end of a shim. This mechanism forces elastomer of the cover layer to expand outward and, due to the nearly incompressible nature of the material, experience lateral contraction of approx. 50 %. Extreme local deformation causes tension both in horizontal and in thickness direction. This creates locally high hydrostatic tension despite an acting compressive stress in vertical direction.

Figure E-29 and Figure E-30 show the magnitude of obtained hydrostatic stress = mean normal stress in tension at $\sigma = 0.52\,GS$ and $\sigma = 1.02\,GS$, respectively. Areas with compressive mean normal stress are shown in dark grey (largest contiguous area).

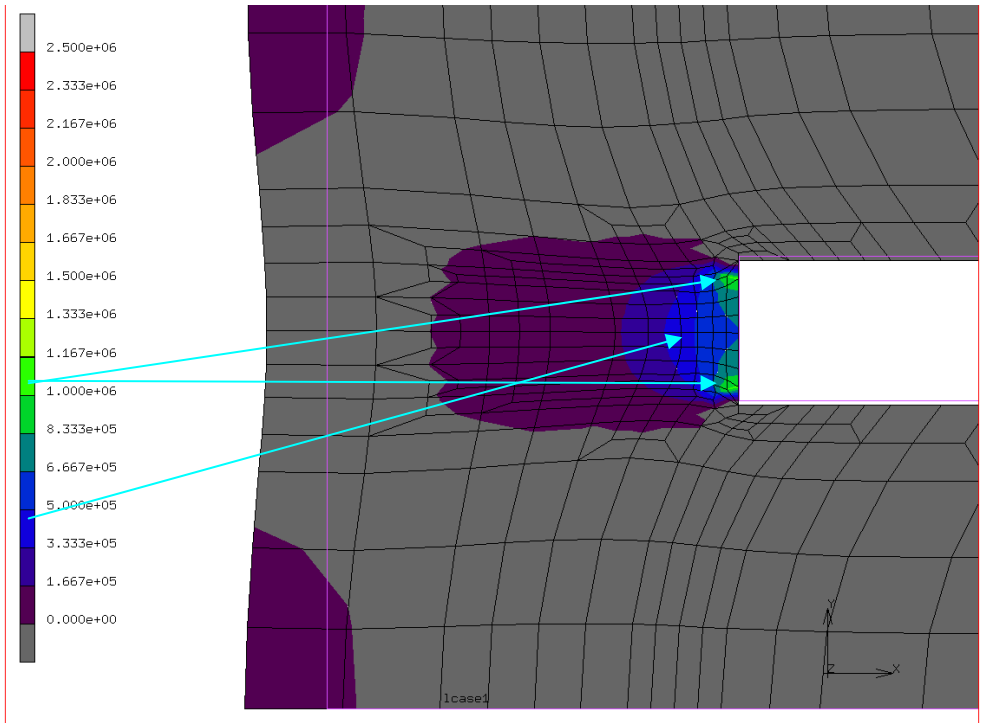

Figure E-29 Computed hydrostatic stress σ_0 in (Pa) at $\sigma = 0.52\,GS$ at the edge of a steel shim.

The amount of material subjected to hydrostatic tension is larger at $\sigma = 0.52\,GS$ (Figure E-29) and shrinks as loading progresses to $\sigma = 1.02\,GS$ (Figure E-30). The intensity of the hydrostatic tension, σ_0, however, increases as the applied load increases. At $\sigma \approx 1.02\,GS$ the hydrostatic tension at the end of the shim reaches the magnitude of $\sigma_0 \approx E \approx 3G$. Gent & Lindley (1959) showed that internal rupture of elastomers nucleates before this relation is satisfied.

This observation has far reaching consequences since it indicates that delamination of the cover layer can be initiated by internal rupture of the elastomer rather than an adhesive bond failure at the interface between elastomer and steel. Visually, the failure mechanism may still be observed as delamination since the highest hydrostatic tension is observed in close proximity of the interface.

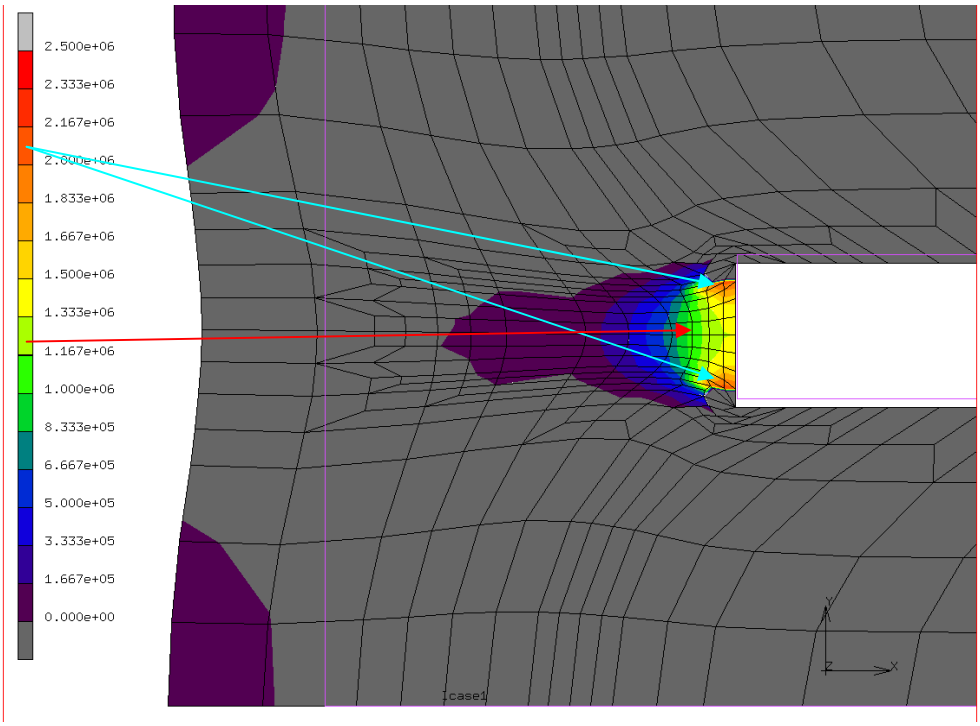

Figure E-30 Computed hydrostatic stress σ_0 in (Pa) at $\sigma = 1.02\,GS$ at the edge of a steel shim.

The intensity of local hydrostatic tension and of local extreme shear strains remains linked to the shear strain in the elastomer at the interface to the steel shim close to the actual edge. Figure E-31 illustrates the distribution of shear strain in the elastomer along the interface to the steel shim at various load levels.

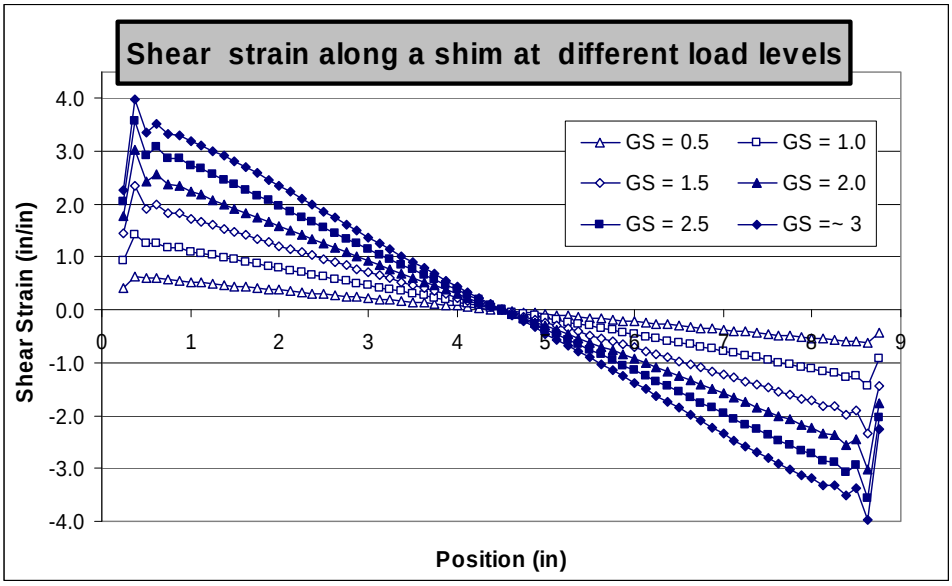

Figure E-31 Shear strain along the shim at different axial loads for a bearing with SF 9

This shows that the shear strain distribution for the inner 95 % of the shim is nearly linear, increasing with the distance from the center of the bearing. It was also found that local effects due to mesh distortion and stress concentration remain local within 1/8" to ¼" from the end of the shim. These two observations motivate the following alternative procedure for the extraction of $\gamma_{zx,\max}$ from the FE analysis:

1. Read the shear strain at a distance of ¼" from the end of the shim.
2. Linearly extrapolate the obtained value to the edge of the shim.

For the analyzed series of bearings, this procedure introduces a scaling factor of $L_{bearing}/(L_{shim} - 2*1/4 \text{ in}) = 1.125$.

E.4.2 Shear Strain Coefficient C_{azzx} for Axial Loading

As discussed in subsection E.4.1, the numerical analysis cannot directly provide the local shear strain at the very end of the shim. Instead, a shear strain at a distance of ¼" behind the end is recorded from the FEA and extrapolated to the end of the shim. For the given bearing, and for axial loading without rotation, the extrapolation is performed by a multiplicative factor of $L_{bearing}/(L_{shim} - 2*1/4 \text{ in}) = 1.125$. The extrapolated data was used to compute the equivalent stiffness coefficient C_{azzx} as

$$C_{azzx} = \frac{\gamma_{zx,\max}}{|\varepsilon_{az}| S} \tag{E-14}$$

with $\gamma_{zx,\max}$ as the maximum shear strain at the end of the shim, ε_{az} as the average axial strain, and shape factor *S*.

The maximum shear strain $\gamma_{zx,\max}$ cannot be extracted directly from the FE analysis since the end of the shim induces a singularity, and as such cannot be assessed numerically.

E.4.2.1 Strip-bearing with SF 6

Figure E-32 shows the obtained value for C_{azzx} as well as the theoretical value after Stanton & Lund (2004) for a bearing with SF 6 over the applied load range. (Normalized as $P/GS\,A = \sigma/GS$.)

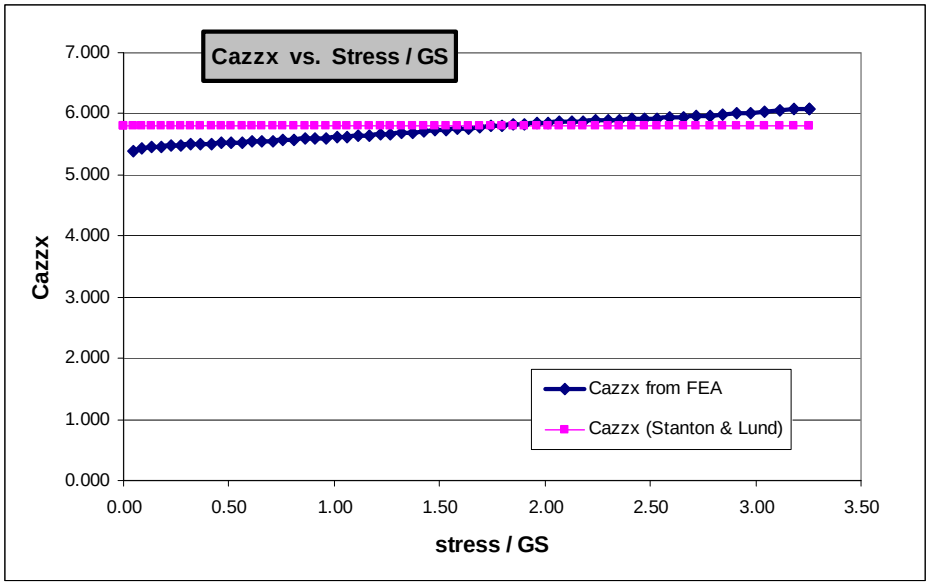

Figure E-32 C_{azzx} **versus** σ / GS **for bearing with SF 6**

E.4.2.2 Strip-bearing with SF 9

Figure E-33 shows the obtained value for C_{azzx} as well as the theoretical value after Stanton & Lund (2004) for a bearing with SF 9 over the applied load range. (Normalized as $P / GS\, A = \sigma / GS$.)

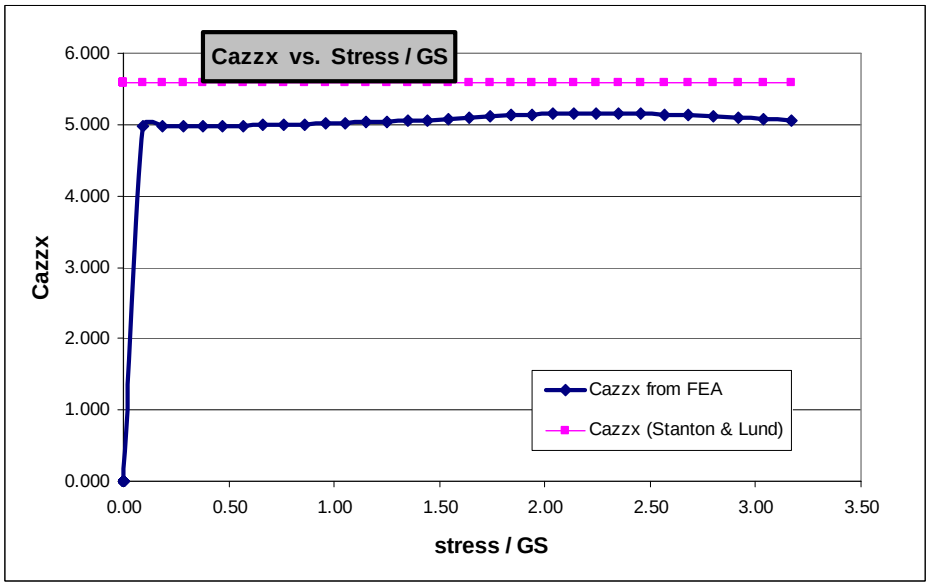

Figure E-33 C_{azzx} **versus** σ / GS **for bearing with SF 9**

E.4.2.3 Strip-bearing with SF 12

Figure E-34 shows the obtained value for C_{azzx} as well as the theoretical value after Stanton & Lund for a bearing with SF 12 over the applied load range. (Normalized as $P/GS\,A = \sigma/GS$.)

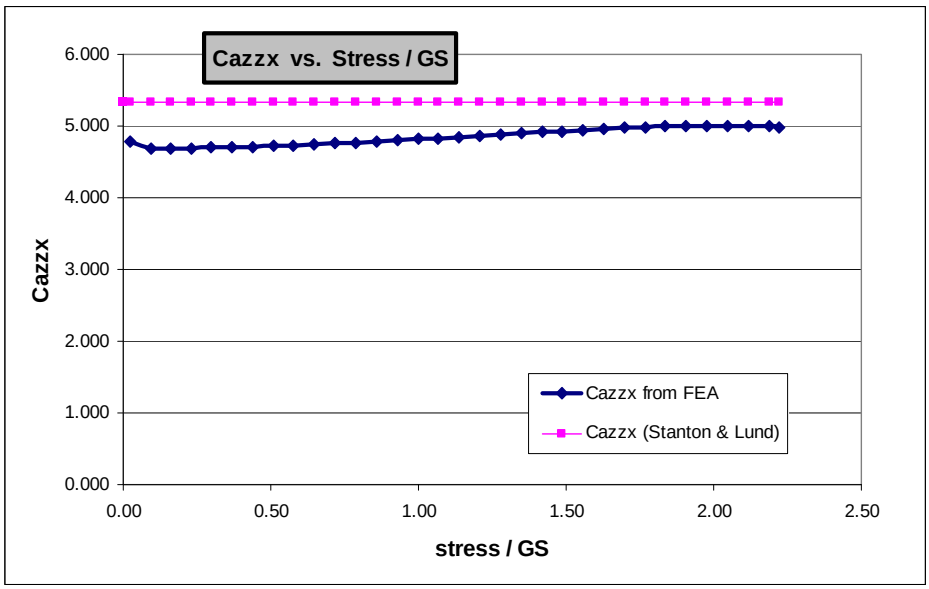

Figure E-34 C_{azzx} **versus** σ/GS **for bearing with SF 12**

The difference between the presented numerical analyses and the respective theoretical values remains below 7.5 %. The difference can be attributed to the error introduced by the simplifying assumption of an isotropic stress state in the theoretical analyses by Gent & Meinecke (1970) as well as Stanton & Lund (2004) versus a general stress state under plane strain conditions in the FEA.

The relatively small model error justifies the use of the theoretical relations for the definition of design strains.

E.4.3 Shear Strain Coefficient C_{ryzx} for Rotation Loading

As discussed in the previous subsection E.4.1, the numerical analysis cannot directly provide the local shear strain at the very end of the shim. Instead, a shear strain at a distance of ¼" behind the end is recorded from the FEA and extrapolated to the end of the shim. This poses a difficult problem since the distribution of shear strain along the shim is no longer linear but rather parabolic.

Extrapolation can be based on the location of zero shear strain along the shim, but for load combinations other than pure rotation, that point is moving. For the sake of completeness, this section presents a conservative attempt of extrapolating shear strain due to rotation to the end of the shims. The results have to be viewed under consideration of a likely error due to the employed procedure. Section E.5 will present an alternative

approach which does not utilize extrapolation and thus does not suffer from the discussed shortcomings.

The extrapolated data was used to compute the equivalent stiffness coefficient C_{ryzx} as

$$C_{ryzx} = \frac{2(\gamma_{zx,\max} - C_{azzx} S|\varepsilon_{az}|)}{S\,l} \frac{\sum t}{\theta_y}, \qquad \text{(E-15)}$$

with $\gamma_{zx,\max}$ as the extrapolated maximum shear strain at the end of the shim, the axial shear strain coefficient C_{azzx} according to Stanton & Lund (2004), the average axial strain ε_{az}, the total rotation θ_y, the layer thickness *t*, and shape factor *S*. In addition to the required extrapolation, equation (E-15) requires separation of shear strain contributions due to axial compression and due to rotation, a procedure which yet needs to be proven suitable for the given problem.

Figure E-35 shows a comparison of back-calculated values for the rotational stiffness coefficient B_{ry} according to (E-13), the shear strain coefficient C_{ryzx} according to (E-15), and the coefficient

$$D_{ryzx} = \frac{C_{ryzx} S}{A_{ry} + B_{ry} S^2} \qquad \text{(E-16)}$$

which links local shear strain to the moment applied to the bearing as

$$\gamma_{zx,\max} = D_{ryzx} \frac{M\,l}{2\,EI}. \qquad \text{(E-17)}$$

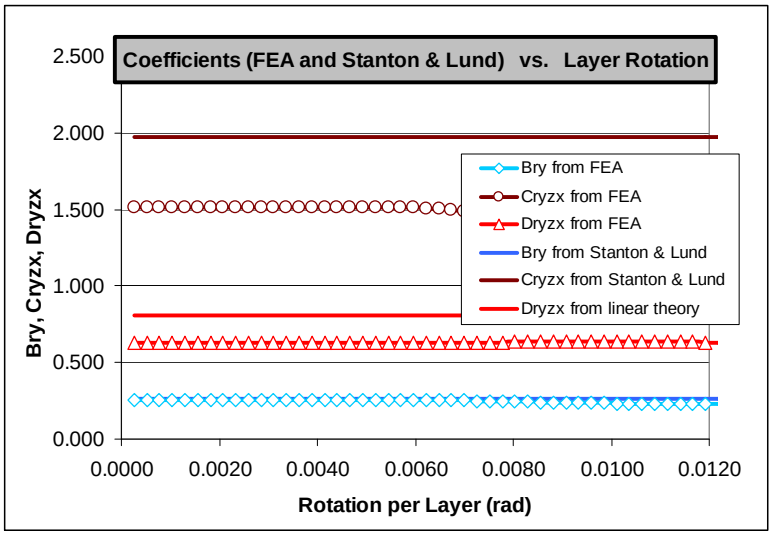

Figure E-35 Coefficients for bearing with SF 9

The comparison of back-calculated values from the FEA and those values obtained from the linear theory shows reasonably good correlation for the stiffness coefficient B_{ry}. The shear strain coefficients C_{ryzx} and D_{ryzx}, however show significant differences. This has to be attributed to the extrapolation of numerically obtained data and the approximate separation of axial and rotational contribution to the local shear strain. Due to the unreliable nature of the procedure outlined in this subsection, no further analysis of this type was performed for bearings with different shape factor. Instead, an alternative procedure was developed to verify the basic hypothesis that superposition remains valid at reasonably small error. This procedure and the obtained results will be discussed in section E.5

E.4.4 Effect of lift-off on the local shear strain

Another important piece of information regarding the relationship between applied angle of rotation and local shear strain is the effect of lift-off at low to moderate axial loads. This information was obtained from studying load combinations where a bearing is first loaded by an axial load and subsequently exposed to an increasing rotation. Force, moment, local strain, and length of lift-off was recorded.

Figure E-36 and Figure E-37 show the distribution of shear strain along the interface of elastomer and shim at various angle of rotation. Figure E-36 is based on an initial axial load level of $\sigma = 0.25\ GS$. Figure E-37 is based on an initial axial load level of $\sigma = 0.50\ GS$.

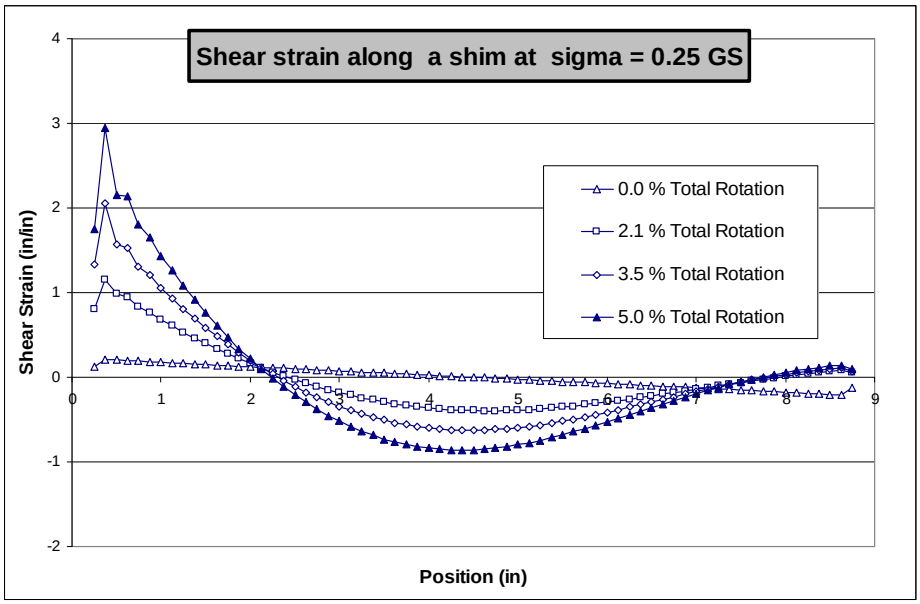

Figure E-36 Shear strain along a shim of a 3-layer bearing with SF 9: Axial load level $\sigma = 0.25\ GS$ **and total rotation** $\theta = 0.0 / 2.1 / 3.5 / 5.0\,\%$

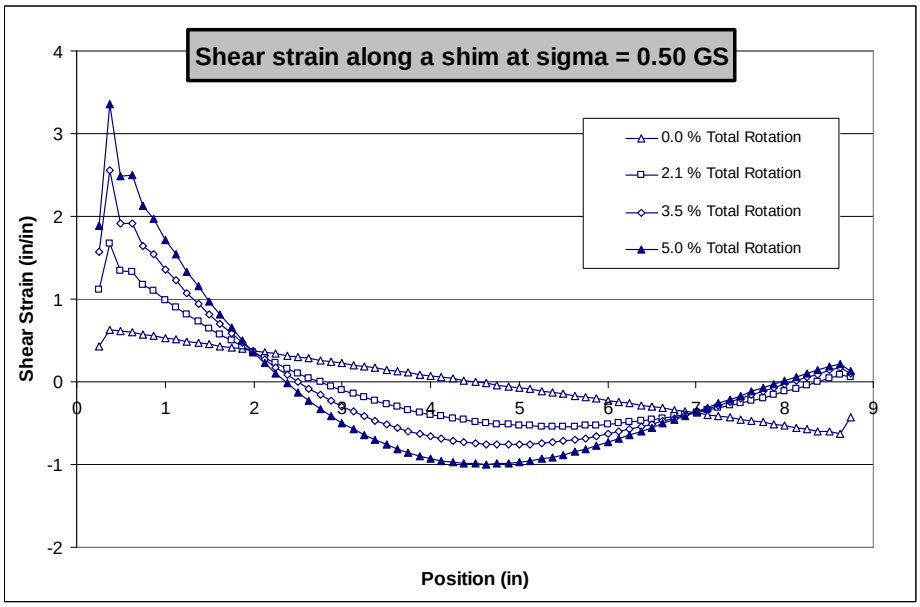

Figure E-37 Shear strain along a shim of a 3-layer bearing with SF 9: Axial load level $\sigma = 0.50\ GS$ **and total rotation** $\theta = 0.0 / 2.1 / 3.5 / 5.0\,\%$

Both figures show the approximately parabolic distribution of shear strain due to the applied rotation as predicted by Stanton & Lund (2004). Deviation from the parabolic distribution on the left end of the plots is due in part to local effects near the end of the shim, and in part due to the observed significant mesh distortion in that area.

Furthermore, both diagrams show proportionally increasing shear strain over the left portion of the bearing (over-compressed by the rotation) as the applied rotation increases,

but reach an ultimate state on the right side of the bearing. Analyzing the deformed shape of the analyzed load combinations reveals that both combinations ultimately experience lift-off. At both load levels, lift-off occurs over a length of ≈ 3 in from the right (Figure E-36 and Figure E-37). Even though the amount of lift-off is approximately the same under both load combinations, the observed ultimate shear strain in those areas differs depending on axial load intensity. Thus, the amount of lift-off by itself does not control this ultimate shear strain.

Analyzing the amount of lift-off versus rotation per layer at different load levels provides the explanation. Figure E-38 shows the ratio of the length of the lift-off area over the total length of the bearing. The amount of lift-off increases as the applied rotation increases and appears to approach an ultimate limit. That limit is controlled by the employed displacement controlled loading. (Discussed in section E.2.2.) However, lift-off starts at increasing rotation angles as the axial load intensity increases.

No lift-off is observed in any numerical simulation with $\sigma > 1.2\ GS$. This does not state that no lift-off occurs above $\sigma > 1.2\ GS$ in real bearings, but that at higher load levels the inevitable element distortion causes the numerical analysis to terminate at a rotation of approx. 0.006 radians/layer, i.e., before lift-off can be observed.

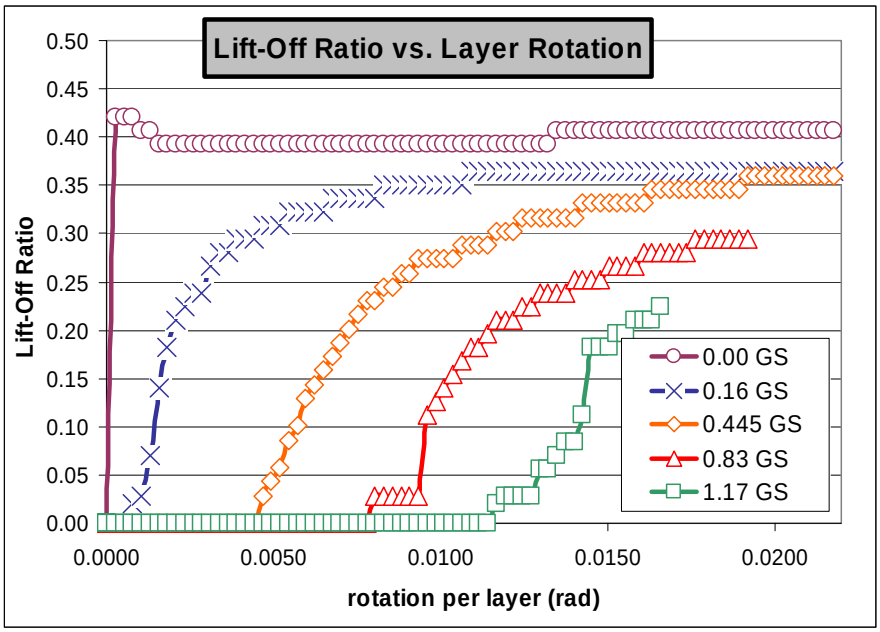

Figure E-38 Lift-off ratio versus rotation per layer for SF 9 bearing at various load levels

The magnitude of the ultimate shear strain in the areas of uplift is approximately the observed magnitude of shear strain at the start of lift-off. Additional shear strain from rotation increments applied after lift-off was initiated affect mainly that part of the bearing under the loaded surface. This generates nonlinear behavior solely on a geometric basis.

Due to the displacement-controlled nature of the simulation, lift-off not only increases the eccentricity of the axial force on the bearing but also its magnitude. This causes the present FEA to underestimate the amount of lift-off on a real bearing.

E.4.5 Bearings with Bonded External Plates – Uplift

Bearings with bonded external plates are used where lift-off cannot be permitted, or where low axial forces cannot provide sufficient friction to hold the bearing in place if it is subjected to shear forces. These bearings do not experience the nonlinear geometric effect as observed in bearings with lift-off. A problem which can arise in bearings with bonded external plates is the presence of hydrostatic tension in parts of the bearing other than the already discussed local hydrostatic tension at the end faces of steel shims. This phenomenon becomes most significant under load combinations where conventional elastomeric bearings would experience lift-off. There is no difference between bearings with or without bonded external plates prior to lift-off.

The aim of this section is to assess the magnitude of hydrostatic tension which might be observed in a bearing with bonded external plates. All presented results within this section are for a strip-bearing with shape factor SF 9. Since all FEA were performed using metric units, the hydrostatic stress data (= mean normal stress) presented in Figure E-39, Figure E-40, and Figure E-41 is given in Pascal (Pa). Gent & Lindley (1959) identified a hydrostatic stress of $\sigma_0 \approx E$ as critical for internal rupture of rubber. With $E = 300$ psi $= 2.07 * 10^6$ Pa, the stress scale in Figure E-39, Figure E-40, and Figure E-41 is set such that the shown maximum intensity represents $\sigma_0 \approx E$ (top end of the scale). Areas with compressive hydrostatic stress and hence without risk of internal rupture are shown in grey (largest contiguous area).

Figure E-39 shows the distribution of tensile hydrostatic stress over the cross section of a bearing subjected to an average axial stress of $\sigma = 0.00\ GS$ and subsequent rotation by $\theta_y = 0.0060$ radians/layer. The entire right half of the bearing is subjected to hydrostatic tension, with a maximum approximately 2 inches inside from the right side surface. The maximum magnitude reaches $\sigma_0 \approx E$ at $\theta_y = 0.0060$ (increment 83). The linear analysis and the numerical solution by FEA are in perfect agreement, both regarding location and magnitude of the hydrostatic tension. The latter can be verified through Figure E-42. A bearing subjected to such loading conditions is most likely to fail due to internal rupture on the side of uplift.

Figure E-40 shows the distribution of tensile hydrostatic stress over the cross section of a bearing subjected to an average axial stress of $\sigma = 0.16\ GS$ and subsequent rotation of $\theta_y = 0.0060$ radians/layer. Approximately $2/3^{rd}$ of the right half of the bearing is subjected to hydrostatic tension, with a maximum approximately 1.4 inches inside from the right side surface. The maximum magnitude reaches $\sigma_0 \approx 0.6E$ at $\theta_y = 0.0060$ (increment 83). A bearing subjected to such loading conditions is unlikely to fail due to internal rupture of the elastomer.

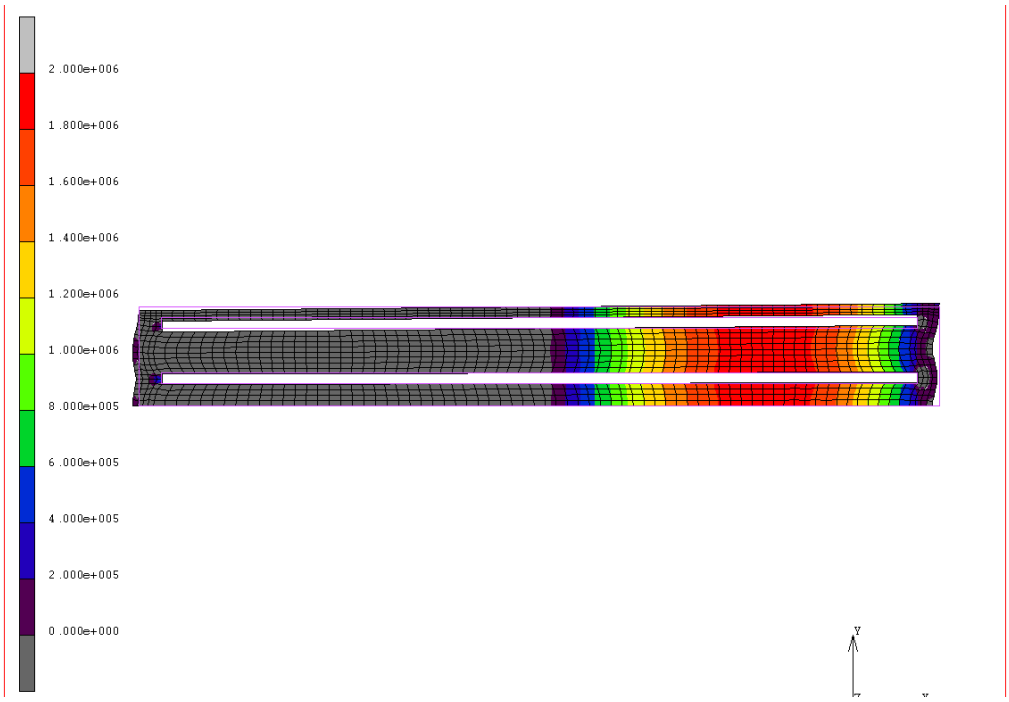

Figure E-39 Tensile hydrostatic stress in (Pa) for $\sigma = 0.00\ GS$ and $\theta_y = 0.0060$ rad/layer

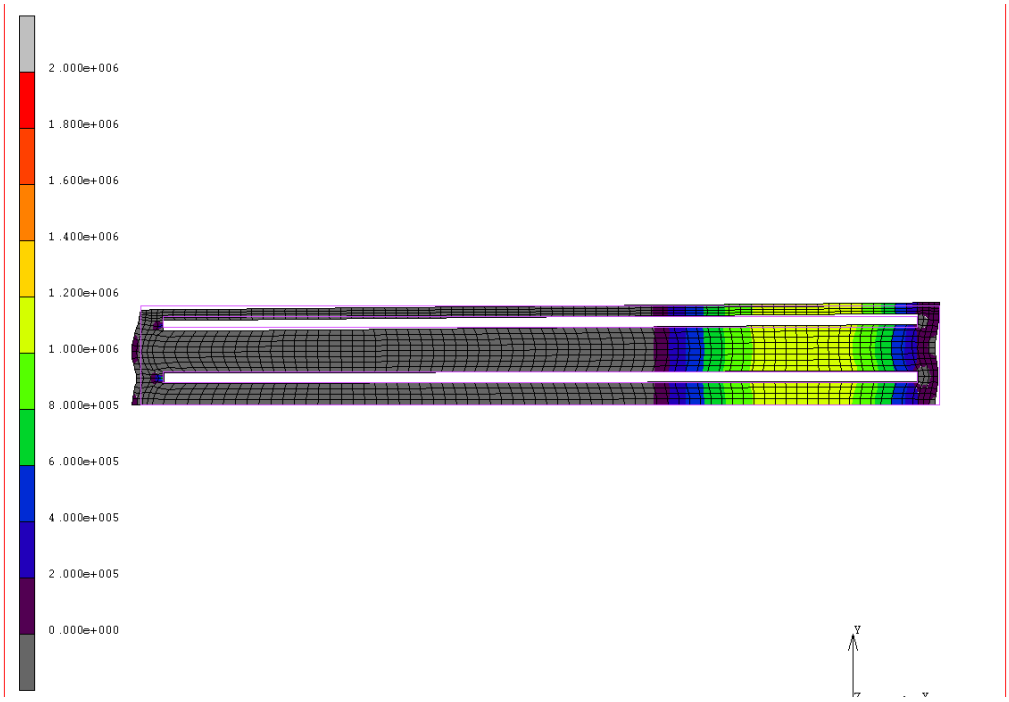

Figure E-40 Tensile hydrostatic stress in (Pa) for $\sigma = 0.16\ GS$ and $\theta_y = 0.0060$ rad/layer

Figure E-41 shows the distribution of tensile hydrostatic stress over the cross section of a bearing subjected to an average axial stress of $\sigma = 0.445\ GS$ and subsequent rotation by $\theta_y = 0.0060$ rad/layer. Only the rightmost 1 inch of the bearing experience hydrostatic tension of $\sigma_0 \le 0.1E$ within the elastomer layer. Significant tensile hydrostatic stress is observed only in the immediate vicinity of the side faces of the center shim. The mesh in that area, however, is too coarse to capture such local phenomena at sufficient accuracy. The local phenomenon at the end of the shims was discussed previously in section E.4.1. It is not considered intrinsic to uplift.

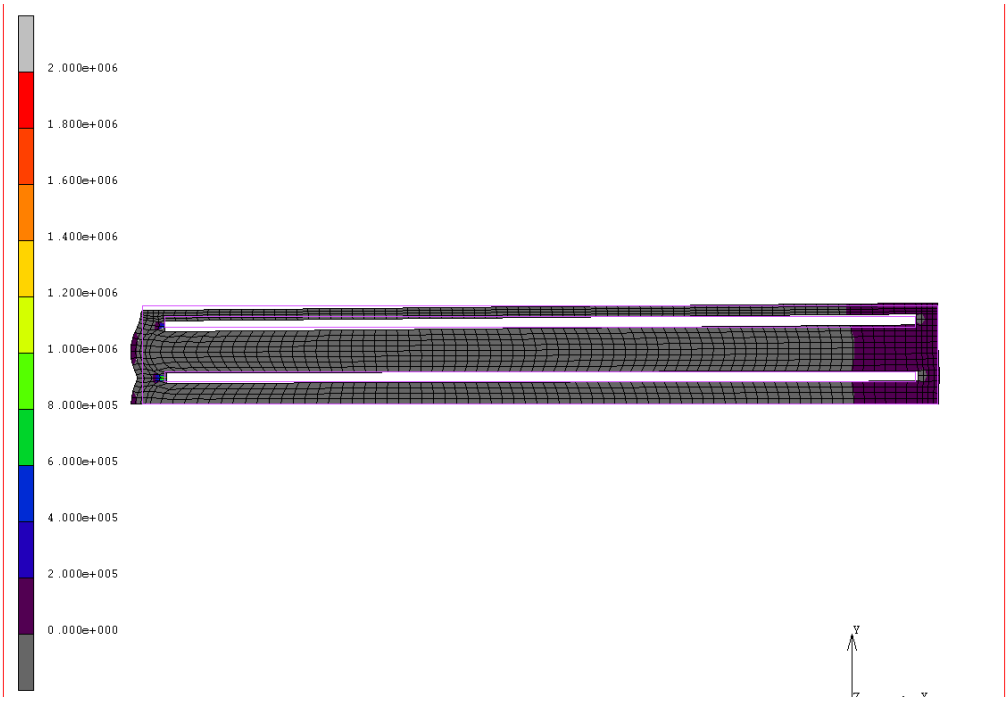

Figure E-41 Tensile hydrostatic stress in (Pa) for $\sigma = 0.445\ GS$ and $\theta_y = 0.0060$ rad/layer

Figure E-41 clearly proves that the risk of internal rupture diminishes rapidly with increasing axial loads. Even axial load levels as low as $\sigma = 0.445\ GS$ practically rule out internal rupture of the elastomer as cause of failure. Only large rotation at axial load levels below $\sigma = 0.2\ GS$ possess real potential for this failure mode.

Figure E-42, Figure E-43, and Figure E-44 show history plots for the hydrostatic stress (= mean normal stress) versus the load increment ID for the same three axial load intensities as used in the respective Figure E-39, Figure E-40, and Figure E-41. This enables easy correlation between the stress distribution images (all taken at increment 83). Increment IDs 60-90 map linearly onto rotations $\theta_y = 0.000 - 0.00778$ rad/layer. Each figure contains the stress history for 5 nodes, each located on a vertical section 2 inches to the left of the right side surface of the bearing. These nodes are evenly spaced across the elastomer layer and including the interface to the top and bottom shim, respectively.

All three figures show a nearly perfect linear relation between hydrostatic stress and applied rotation for $\theta_y = 0.000 - 0.0060$ rad/layer (increments 60-83). Only above increment 85, the graphs in Figure E-42 exhibit a radical change of behavior. This phenomenon is created by loss of numerical stability of the nearly incompressible finite element and is not of physical but of purely numerical origin. It can be identified simply by visual inspection of the simulated deformed shape of the bearing, where a fast evolving pattern of hourglass modes appears. This numerical limit restricts the range of reliably simulated rotations to $|\theta_y| \le 0.0060$ rad/layer.

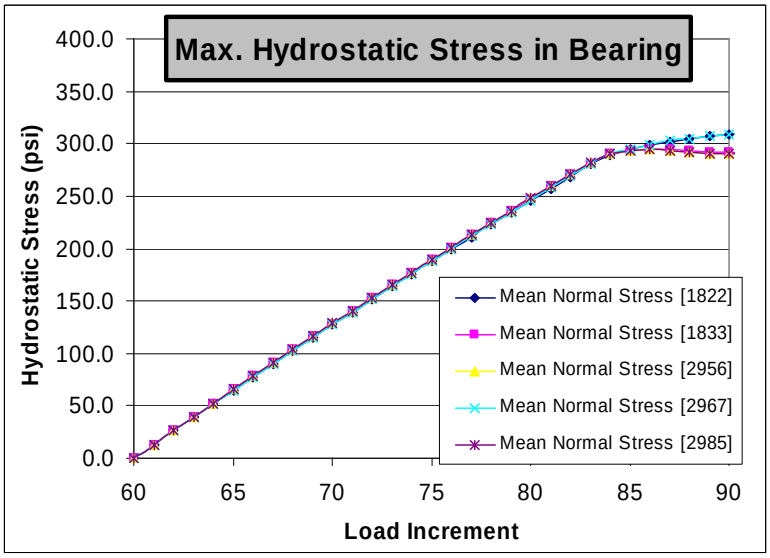

Figure E-42 History of hydrostatic stress in (psi) for $\sigma = 0.00\ GS$ (Increments 60-90)

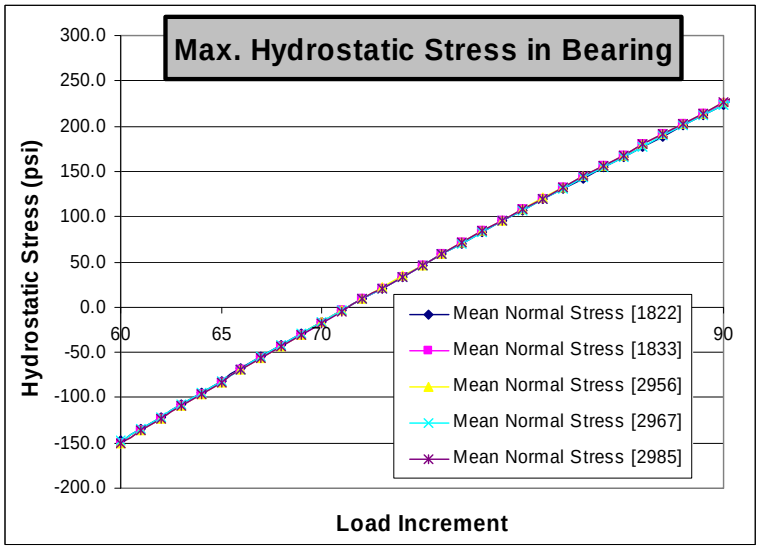

Figure E-43 History of hydrostatic stress in (psi) for $\sigma = 0.16\ GS$ (Increments 60-90)

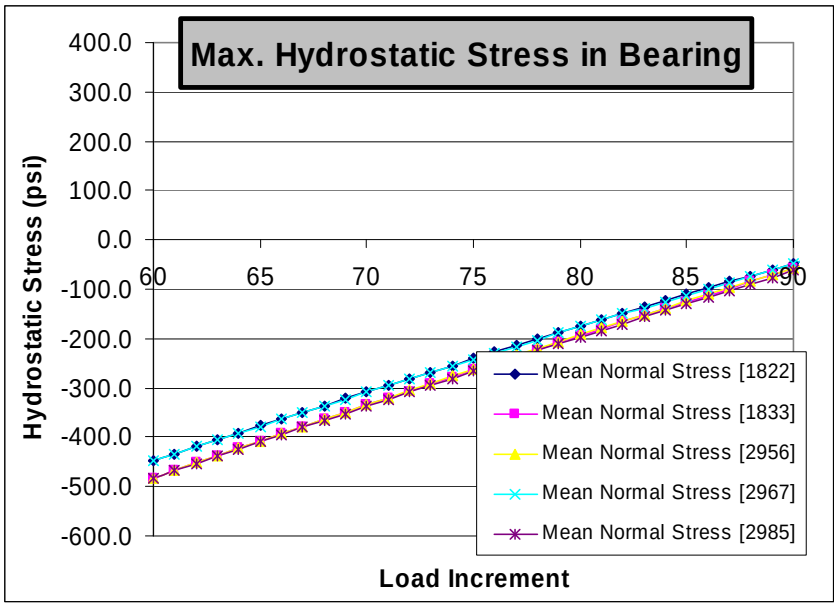

Figure E-44 History of hydrostatic stress in (psi) for $\sigma = 0.445\ GS$ (Increments 60-90)

The simulation proves that within the suitable range of $|\theta_y| \le 0.0060$ rad/layer,

1. the hydrostatic stress for any given point is linearly related to the applied rotation, and that

2. the hydrostatic stress is nearly constant across the thickness of the elastomer layer.

Statement 1 is crucial for the applicability of the linear theory by Stanton & Lund (2004). It proves that the linear theory can be used to assess the magnitude of hydrostatic stress in bearings with bonded external plates.

Statement 2 also supports the linear theory by Stanton & Lund by proving their basic assumption of a hydrostatic stress state within the elastomer to be correct. This does not hold at higher axial load intensities $\sigma > 1.0\ GS$. However, the above discussion demonstrated that for $\sigma > 0.5 GS$, hydrostatic tension and internal rupture are not possible for any practically reasonable load combination.

E.5 Model Error – Significance of nonlinear effects and Superposition

One key research question behind the presented numerical analysis concerns the validity of the superposition principle based on the design relations by Stanton & Lund (2004). Strictly speaking, after considering the nonlinear elastic nature of elastomers and the locally large strains as observed near the ends of the steel shims, superposition is not valid for the given problem. However, nonlinear analysis provides the means to quantify the error which is introduced by the use of a linear theory and by application of the superposition principle. The following analysis proves that the error introduced by these assumptions remains within acceptable bounds for all reasonable combinations of axial loads and imposed rotations.

This proof is performed as follows:

1. Verify that the obtained results from nonlinear FEA and those obtained from the linear theory by Stanton & Lund are closely related. This was performed in Section E.3.
2. Represent a characteristic numerical result, e.g. the local shear strain at the end of a shim, as a smooth function of average axial stress and the applied rotation.
3. Extract the linear portion of the function. This represents all possible combinations as characterized by superposition of linear models for axial and rotational behavior.
4. Analyze the difference between both functions, i.e. the error introduced by linearization and superposition. This provides an error map over the entire range of average axial stress and applied rotation.
5. Verify that the obtained model error does not exceed the commonly accepted model errors.

Steps 2 through 5 will be developed and discussed in this section.

The typical results of a finite element analyses are a displacement field, a spatial distribution of stress and strain, and some characteristic functions thereof. A nonlinear analysis provides a sequence of such results for a given load history. Post-processing of numerical results can be performed in a spatial sense at any given time (path plots, or intensity plots), or in an evolutionary sense for any fixed material point (history plots, typically at nodal points).

Assessing the significance of nonlinear behavior requires analysis of numerical data over the given load history (history plots). For elastomeric bearings, the primary numerical information of interest is the maximum local shear strain at the end of each steel shim.

Placed in the space of input parameters for load (or $P/GSA = \sigma/GS$) and rotation per layer ($\theta_L = \theta_y / n$), such a history plot defines a single line. Figure E-45 shows a

collection of results for a SF 9 bearing. Each line represents one nonlinear solution for a given loading history.

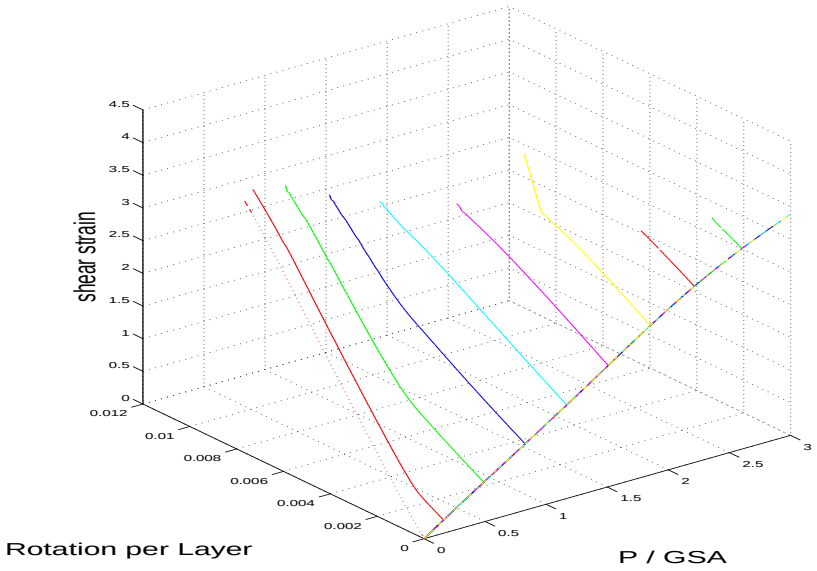

Figure E-45 Collection of resulting shear strain (in/in) from 10 different nonlinear analyses of an elastomeric bearing with SF 9

Such data is difficult to process for information such as load-combinations which cause equivalent $\gamma_{zx,\max}$, or the significance of nonlinear effects. One way to process such simulation data is to perform a least-square fit using higher order polynomial functions. In the present case, the simulation data was fitted by a function of the following type:

$$\gamma_{zx,\max} = \sum_{i=0}^{m}\sum_{j=0}^{m} a_{ij}\left(\frac{\sigma}{GS}\right)^{i}\left(\frac{\theta_y}{n}\right)^{j}, \qquad \text{(E-18)}$$

where i and i were restricted to $i + j \le m$. Using the full series given in (E-18) did not improve the obtained fit or even increased the value of the error function

$$Error = \frac{1}{2}\sum_{k}^{n_{data}}\left((\gamma_{zx,\max})_k - \sum_{i=0}^{m}\sum_{j=0}^{m} a_{ij}\left(\frac{\sigma_k}{GS}\right)^{i}\left(\frac{\theta_{y,k}}{n}\right)^{j}\right)^2. \qquad \text{(E-19)}$$

In (E-19), $\left(\gamma_{zx,\max}\right)_k$, σ_k, and $\theta_{y,k}$ are the maximum shear strain, the average axial stress, and the total rotation on an *n*-layer bearing, respectively, for a single data point *k* from any of the numerical simulations. n_{data} is the total number of such data points on all extracted history series (shown in Figure E-45). The coefficients a_{ij} are obtained from minimizing the error function defined in (E-19).

This fitting analysis was performed for four series of simulations:

1. Strip bearings with SF 6 and bonded external plates. This series creates uplift at larger rotations.

2. Strip bearings with SF 9 and bonded external plates. This series creates uplift at larger rotations.

3. Strip bearings with SF 6 without bonded external plates. This series allows for lift-off with increasing rotation at low axial forces.

4. Strip bearings with SF 9 without bonded external plates. This series allows for lift-off with increasing rotation at low axial forces.

Table E-6 and Table E-7 present the obtained coefficients a_{ij}, listed as a(i,j), for $m = 1,2,3,4$. The residual error follows from (E-19). The relative error is the average error per simulated data point. The grey rows indicate the linear portion of the fit function. The theoretically exact value for a_{00} is zero. By leaving it in the fitting function it provided an additional indicator for the quality of the obtained fit. Both Table E-6 and Table E-7 show that a cubic fit ($m = 3$) does not improve the quality of the quadratic fit ($m = 2$). A fourth-order fit ($m = 4$), however, reduces the residual error by one order of magnitude. Hence, the fourth-order fit is used for further analysis of the simulation data for bearings with bonded external plates.

Table E-6 Coefficients a_{ij} for a bearing with SF 6 and with bonded external plates (creates uplift)

	first order	second order	third order	fourth order
residual error	0.614977	0.176999	0.0429617	0.00282347
relative error	2.90E-04	8.34E-05	2.03E-05	1.33E-06
filter	0.95	0.95	0.95	0.95
a(0,0)	-0.0033718	-0.004127629	0.004038349	7.89336E-05
a(0,1)	99.83018	96.89916	87.27366	94.63276
a(0,2)		-427.5588	436.738	-533.9755
a(0,3)			-24699.46	2744.619
a(0,4)				306662.2
a(1,0)	1.227283	1.280348	1.217256	1.307392
a(1,1)		8.437844	34.04034	-7.632171
a(1,2)			-838.0112	2671.265
a(1,3)				-63230.05
a(2,0)		-0.04531494	0.007186415	-0.1871607
a(2,1)			-10.65604	28.63141
a(2,2)				-1622.822
a(3,0)			-0.009633514	0.1255976
a(3,1)				-9.693649
a(4,0)				-0.03011815

Table E-7 Coefficients a_{ij} for a bearing with SF 9 and with bonded external plates (creates uplift)

	first order	second order	third order	fourth order
residual error	2.27244	0.632014	0.205623	0.056222
relative error	1.23E-03	3.43E-04	1.12E-04	3.05E-05
filter	0.95	0.95	0.95	0.95
a(0,0)	0.01290003	-0.007826721	0.004587233	0.000589096
a(0,1)	190.3133	213.4127	187.5294	202.3827
a(0,2)		-4017.144	-1188.889	-2547.037
a(0,3)			-234146.8	-602006.8
a(0,4)				5017239
a(1,0)	1.218682	1.307256	1.150499	1.267248
a(1,1)		12.40025	94.84205	-6.176302
a(1,2)			-1437.27	17600.93
a(1,3)				-181350.8
a(2,0)		-0.04788143	0.1149509	-0.110806
a(2,1)			-43.69741	22.84785
a(2,2)				-9752.122
a(3,0)			-0.03943107	0.09635822
a(3,1)				-7.070999
a(4,0)				-0.02552705

Table E-8 and Table E-9 provide the coefficients for fitting data from series 3 and 4. These series differ from those used for Table E-6 and Table E-7 by the fact that series 1 and 2 include bonded external plates while simulations of series 3 and 4 do not have bonded external plates and thus show lift-off at low axial load. Table E-8 shows that a cubic fit ($m = 3$) does improve the quality of the quadratic fit ($m = 2$), almost to the level of a fourth-order fit ($m = 4$). Table E-9 shows the same trend as observed in bearings with bonded external plates. (Compare Table E-6 and Table E-7.) For consistency with the bearings with bonded external plates, the fourth-order fit is used for further analysis of the simulation data for bearings without bonded external plates.

Table E-8 Coefficients a_{ij} for a bearing with SF 6 without bonded external plates (allows lift-off)

	first order	second order	third order	fourth order
residual error	1.74733	0.516877	0.168999	0.119117
relative error	8.89E-04	2.63E-04	8.59E-05	6.05E-05
filter	0.95	0.95	0.95	0.95
a(0,0)	-0.01007482	-0.006510036	0.001616491	-0.000855979
a(0,1)	94.23355	88.50083	73.80879	79.26412
a(0,2)		-1057.981	-504.3859	-2112.06
a(0,3)			-49808.31	-68183.09
a(0,4)				485376.7
a(1,0)	1.244375	1.306771	1.271672	1.35963
a(1,1)		18.10389	66.64402	57.6341
a(1,2)			-143.0969	5357.56
a(1,3)				-22222.19
a(2,0)		-0.06390393	-0.08245211	-0.3462506
a(2,1)			-25.20037	-39.19804
a(2,2)				-2554.959
a(3,0)			0.02386593	0.2663517
a(3,1)				10.01065
a(4,0)				-0.06752026

Table E-9 Coefficients a_{ij} for a bearing with SF 9 without bonded external plates (allows lift-off)

	first order	second order	third order	fourth order
residual error	3.92332	1.17059	0.632986	0.495678
relative error	2.21E-03	6.60E-04	3.57E-04	2.79E-04
filter	0.95	0.95	0.95	0.95
a(0,0)	0.006298161	-0.007256052	0.00325945	0.000250963
a(0,1)	180.5578	182.9504	148.7345	172.6307
a(0,2)		-4341.195	-3437.645	-15751.6
a(0,3)			-164318.4	-177393.2
a(0,4)				42724700
a(1,0)	1.230061	1.313274	1.174864	1.280184
a(1,1)		37.60824	153.109	125.8076
a(1,2)			-1231.523	31999.2
a(1,3)				-1394922
a(2,0)		-0.05232264	0.08770535	-0.1379262
a(2,1)			-58.91758	-105.4658
a(2,2)				-8694.133
a(3,0)			-0.03263682	0.1138073
a(3,1)				23.18539
a(4,0)				-0.02891924

The obtained fitting functions allow for smooth interpolation between simulated data. Moreover, it can be used to construct contours (iso-lines) of constant local shear strain. Figure E-46 to Figure E-49 show the obtained fourth-order fit functions and contour lines for bearings with SF 6 and SF 9, with and without bonded external plates. The left image in each figure shows the relation in a 3D plot, together with the simulated data (visible as curves on the fitted surface), and the obtained contour lines (equal local shear strain). The right images show the projection of the simulated data curves and the contour lines for local shear strain in (in/in).

Due to the inevitable mesh distortion at large local strains and the problem of hourglass modes at high hydrostatic tension, reliable simulation data does not cover the entire parameter space of axial loading ($P/GSA = \sigma/GS$) and rotation per layer ($\theta_L = \theta_y / n$). This is visible at ratios $P/GSA = \sigma/GS > 1.5$ and increasing rotation. Contour lines beyond this data range are obtained through extrapolation and have to be viewed with caution.

For bearings with bonded external plates, Figure E-46 and Figure E-47 show an almost linear relation between $P/GSA = \sigma/GS$, $\theta_L = \theta_y / n$, and the local shear strain γ_{zx} over the entire range of practically suitable loads and rotations. Within the presented range, uplift is only observed for $P/GSA = \sigma/GS < 1$.

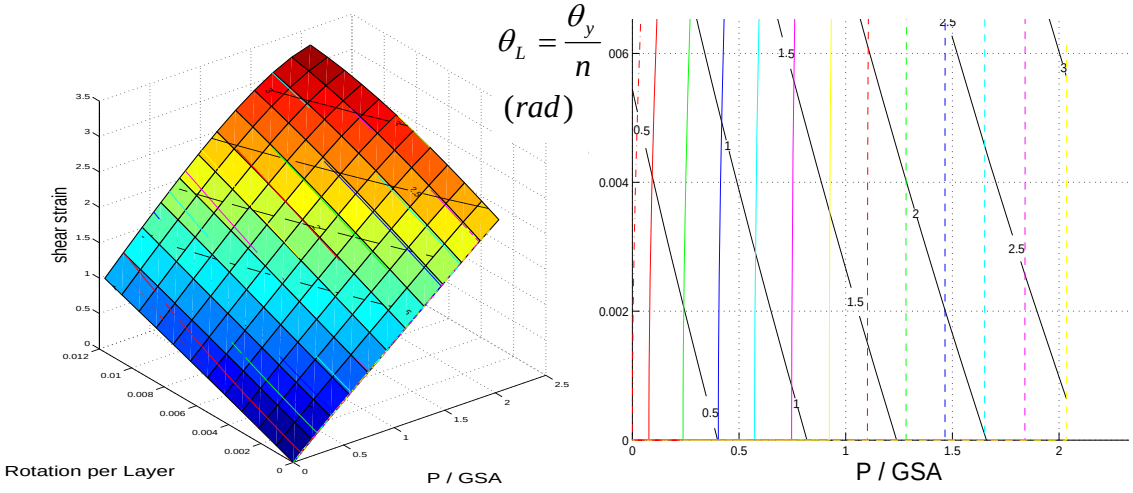

Figure E-46 Fourth-order fit to simulation data for a SF 6 bearing with bonded external plates for shear strain at ¼" distance from the critical edge of the shim. Simulated data (lines/curves), fitted surface (left image), and contour lines for shear strain (in/in).

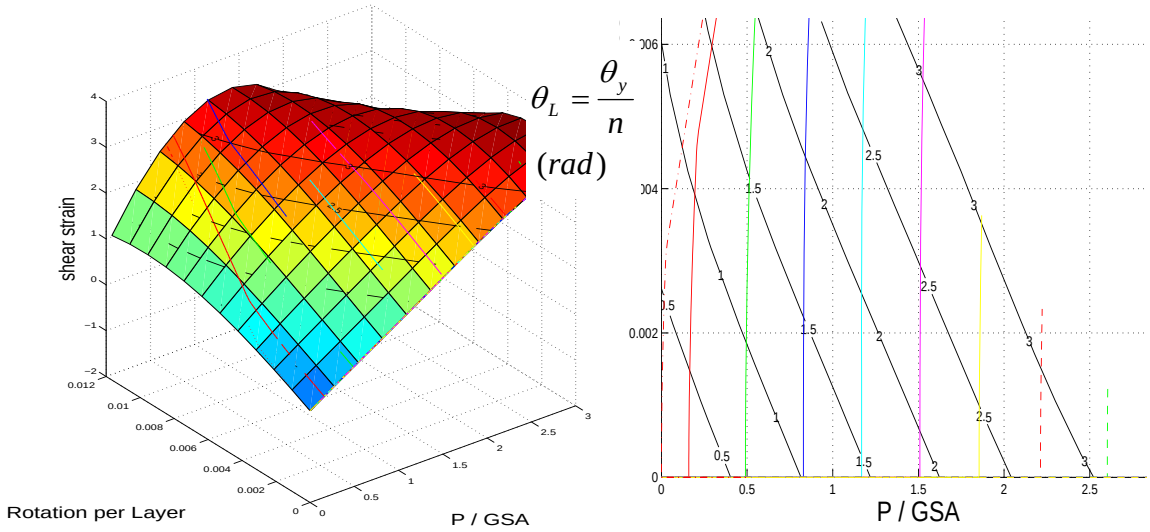

Figure E-47 Fourth-order fit to simulation data for a SF 9 bearing with bonded external plates for shear strain at ¼" distance from the critical edge of the shim. Simulated data (lines/curves), fitted surface (left image), and contour lines for shear strain (in/in).

In bearings without bonded external plates, lift-off is observed instead of uplift at increasing rotation and $P/GSA = \sigma/GS < 1$. This introduces a geometrically driven nonlinearity to the bearing response. Figure E-48 and Figure E-49 show the computed behavior (curves) and the identified smooth fit. Again, the simulated data does not cover the entire parameter space and thus values on the fitted surface for $P/GSA = \sigma/GS >\approx (3 - 250\theta_L)$ represents extrapolation and must not be considered for interpretation.

For both SF 6 and SF 9 an almost linear relation between $P/GSA = \sigma/GS$, $\theta_L = \theta_y / n$, and the local shear strain γ_{zx} is observed over most of the range of practically suitable loads and rotations. However, the relation becomes nonlinear at small axial loads. This reflects the effect of lift-off during rotation at low axial loads.

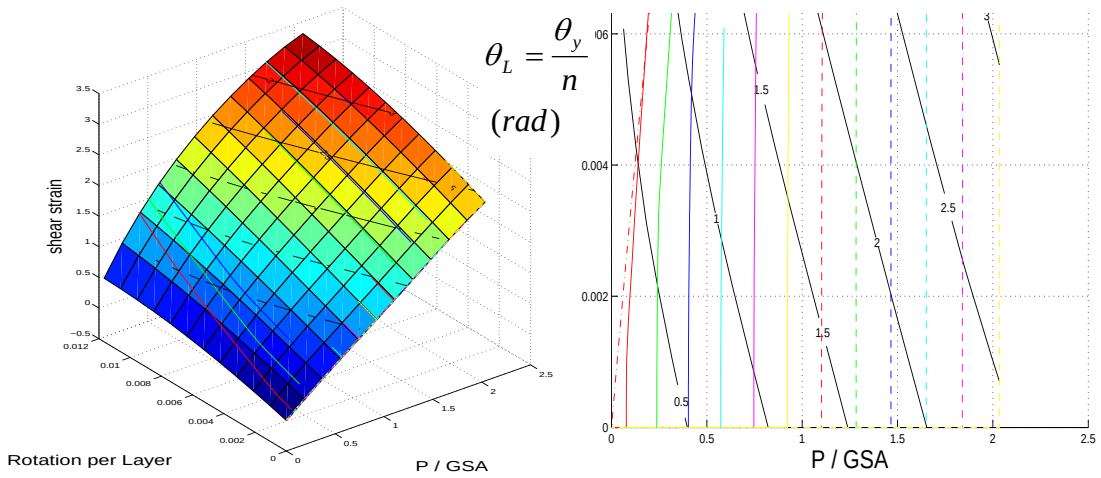

Figure E-48 Fourth-order fit to simulation data for a SF 6 bearing without bonded external plates for shear strain at ¼" distance from the critical edge of the shim. Simulated data (lines/curves), fitted surface (left image), and contour lines for shear strain (in/in).

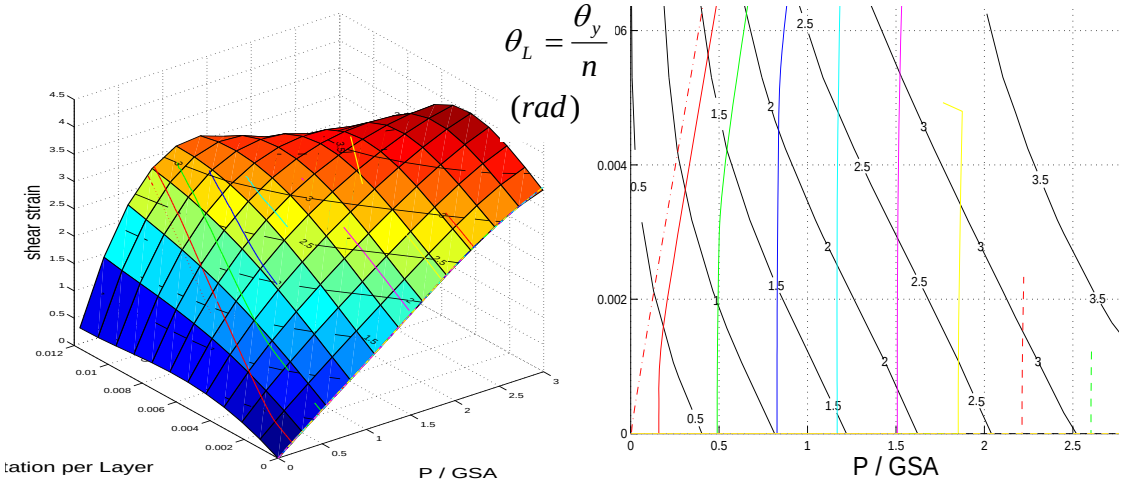

Figure E-49 Fourth-order fit to simulation data for a SF 9 bearing without bonded external plates for shear strain at ¼" distance from the critical edge of the shim. Simulated data (lines/curves), fitted surface (left image), and contour lines for shear strain (in/in).

The smooth fitted function (E-18) with parameters from Table E-6 to Table E-9 provide further insight into the overall behavior and allow further interpretation of the analysis.

Using the linear terms in (E-18), i.e.,

$$\gamma_{zx,\max} = a_{00} + \sum_{i=1,j=1}^{1} a_{ij}\left(\frac{\sigma}{GS}\right)^i\left(\frac{\theta_y}{n}\right)^j = a_{00} + a_{10}\left(\frac{\sigma}{GS}\right) + a_{01}\left(\frac{\theta_y}{n}\right), \qquad \text{(E-20)}$$

provides the ideal approximation of the nonlinear behavior by means of a linear theory of bearing deformation. It is used to identify the significance of using a geometrically and physically nonlinear theory over a much simpler (and thus more usable) linear theory. This significance is measured in terms of a relative error of a linear solution defined as

$$Error_{\mathrm{mod}\,el} = \frac{\left(\gamma_{zx,\max}\right)_{nonlinear} - \left(\gamma_{zx,\max}\right)_{linear}}{\left(\gamma_{zx,\max}\right)_{linear}}. \qquad \text{(E-21)}$$

This error represents a model error or analysis error which affects the computation of maximum shear strain when using a linear analysis model.

Figure E-50 and Figure E-51 show iso-error plots for bearings with bonded external plates for SF 6 and SF 9, respectively, up to load levels of $\sigma / GS \approx 2.5$ and rotations per layer of $\theta_L = 0.006$ *radians*. Figure E-52 and Figure E-53 show the equivalent results for similar bearings without bonded external plates.

Bearings with bonded external plates subjected to rotations typically show a model error below 5 %, reaching maxima around 10 %. (Higher error values in Figure E-51 lie outside the supported domain and represent extrapolations beyond the actual simulations.) The largest model error is observed along the line of pure rotation ($\sigma / GS = 0$).

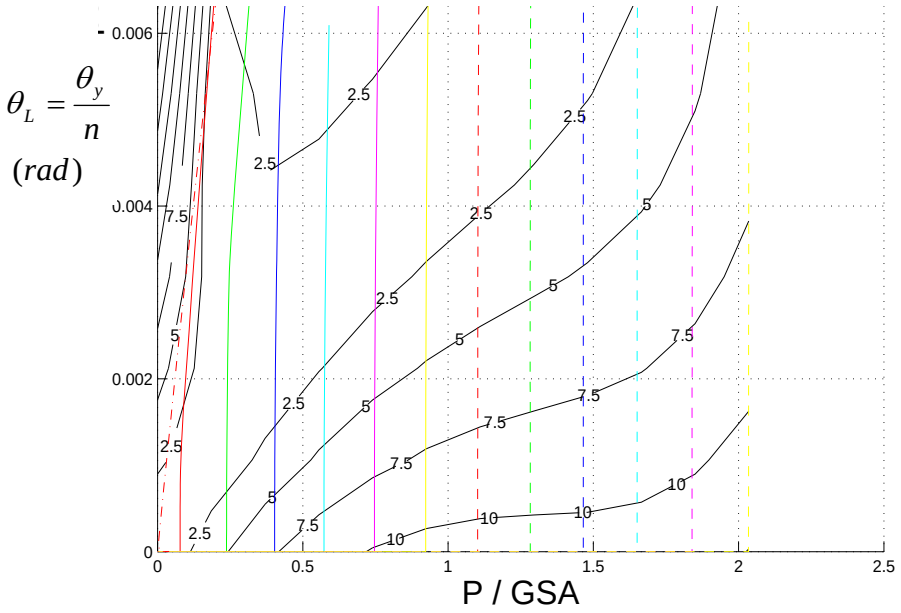

Figure E-50 Iso-error plot for shear strain γ_{zx} for a SF 6 bearing with bonded external plates based on a fourth-order fit. (Constructed for shear strain at ¼" distance from the critical edge of the shim.)

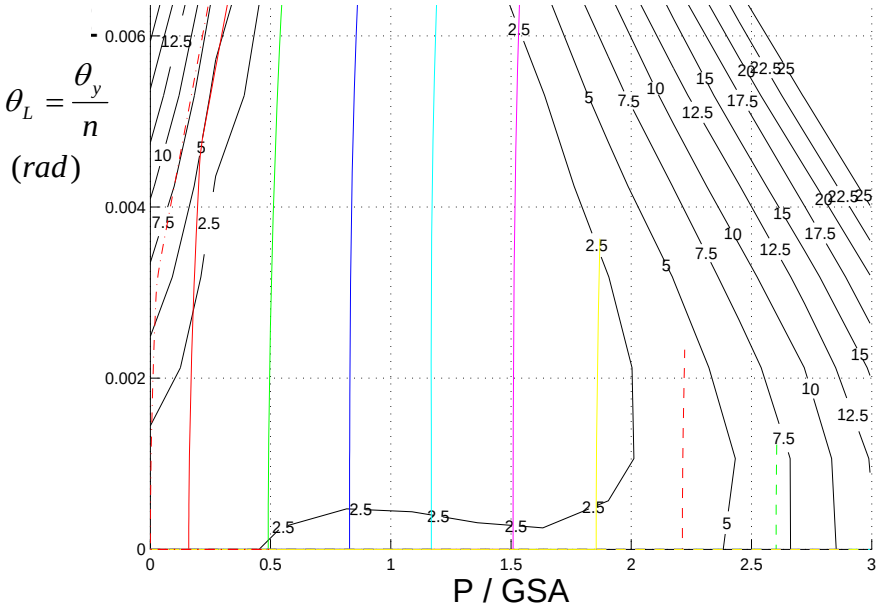

Figure E-51 Iso-error plot for shear strain γ_{zx} for a SF 9 bearing with bonded external plates based on a fourth-order fit. (Constructed for shear strain at ¼" distance from the critical edge of the shim.)

Bearings without bonded external plates experience lift-off at low load levels. This is reflected in the iso-error plots shown in Figure E-52 and Figure E-53. The typical model error lies below 5 %, but reaching maxima above 15 %. At high axial loads, higher error values are observed outside the supported domain and represent extrapolation errors introduced by the fit functions. At low axial force, the higher error value may be affected by extrapolation errors, but are also due to the geometric nonlinearity due to lift-off. This latter contribution has to be addressed in a semi-linear analysis by introducing the amount of lift-off into the analysis. This issue of implementing the effect of lift-off into a semi-linear analysis model will be addressed in greater detail in Appendix F.

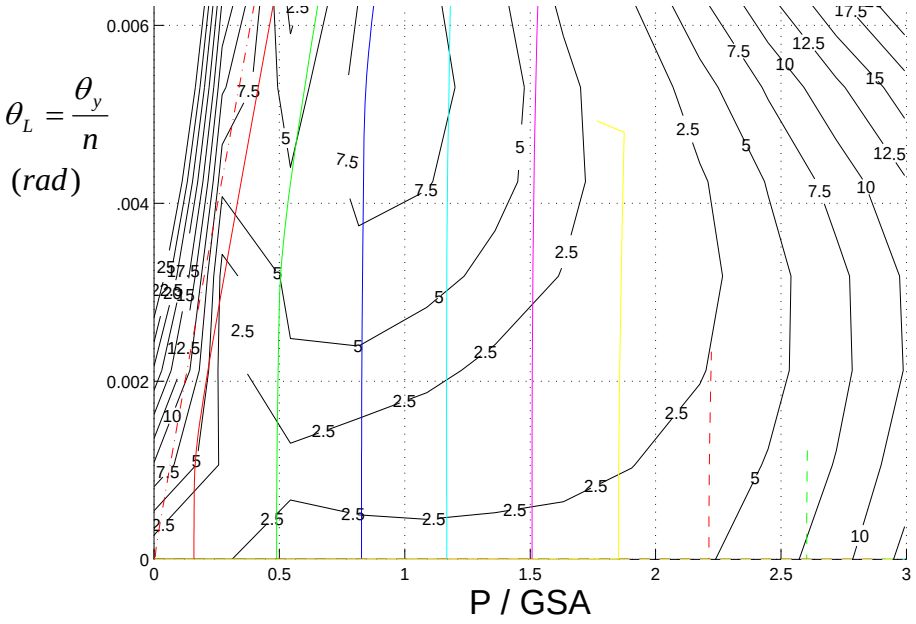

Figure E-52 Iso-error plot for shear strain γ_{zx} for a SF 6 bearing without bonded external plates based on a fourth-order fit. (Constructed for shear strain at ¼" distance from the critical edge of the shim.)

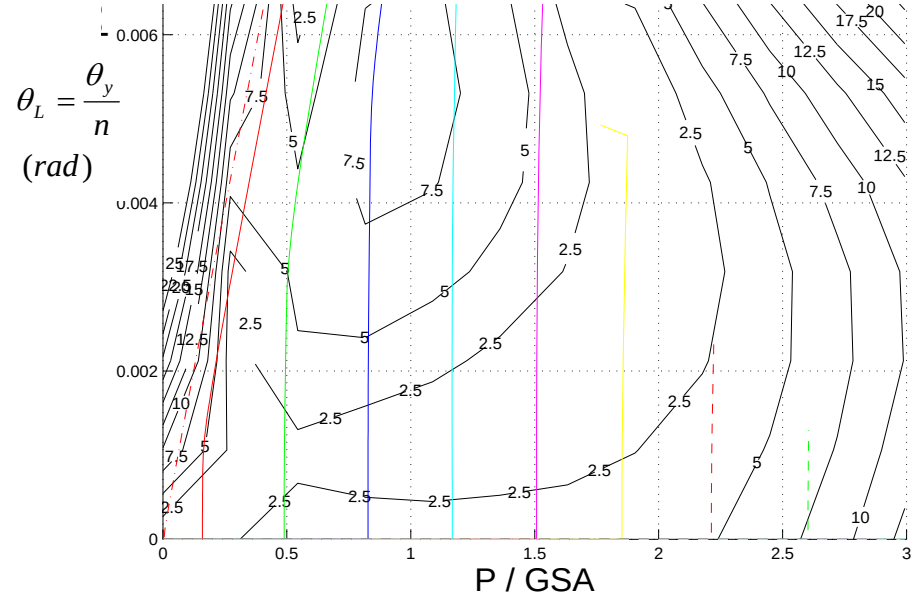

Figure E-53 Iso-error plot for shear strain γ_{zx} for a SF 9 bearing without bonded external plates based on a fourth-order fit. (Constructed for shear strain at ¼" distance from the critical edge of the shim.)

E.6 Conclusions

This chapter presented key results of performed numerical analyses. The extracted information provided proof of the key hypotheses needed for an effective while simple design procedure. In detail, these findings support the following statements.

1. The *stiffness coefficients* predicted by the linear theory of bearings by Stanton & Lund (2004) are in good agreement with a nonlinear FEA and thus provide a simple way to predict axial and rotational stiffness of elastomeric bearings. Typical model errors are below 5-7 %.

2. The *local shear strain* predicted by the linear theory of bearings by Stanton & Lund (2004) is in good agreement with a nonlinear FEA. Typical errors due to spuerposition are in the range of 5-10 %.

3. *Superposition* of axial and rotational effects provides a reasonably accurate representation of the nonlinear FEA. The presented error analysis proved that model errors combined with errors due to superposition are typically below 7.5 %. Only load combinations which cause lift-off were found to reach model errors up to 20 %, thus suggesting modification of Stanton & Lund's relations for bearings with lift-off.

4. Within the investigated load combinations, *Internal rupture* due to excessive tensile hydrostatic stress can only occur in bearings with bonded external plates and low axial load intensities of $\sigma < \approx 0.2GS$.

The relatively small overall error within the common load regime for elastomeric bearings, as identified in section E.5, justifies the use of the linear analysis by Stanton & Lund (2004) for design equations.

Most standard bearings can be designed safely with the worst model error up to 20 % for bearings with limited lift-off permitted. However, for specialty bearings for which lift-off shall be permitted by design, the extra effort for using a more accurate piece-wise linear design analysis can be justified by a reduced model error.